CHALMERS
UNIVERSITY OF TECHNOLOGY

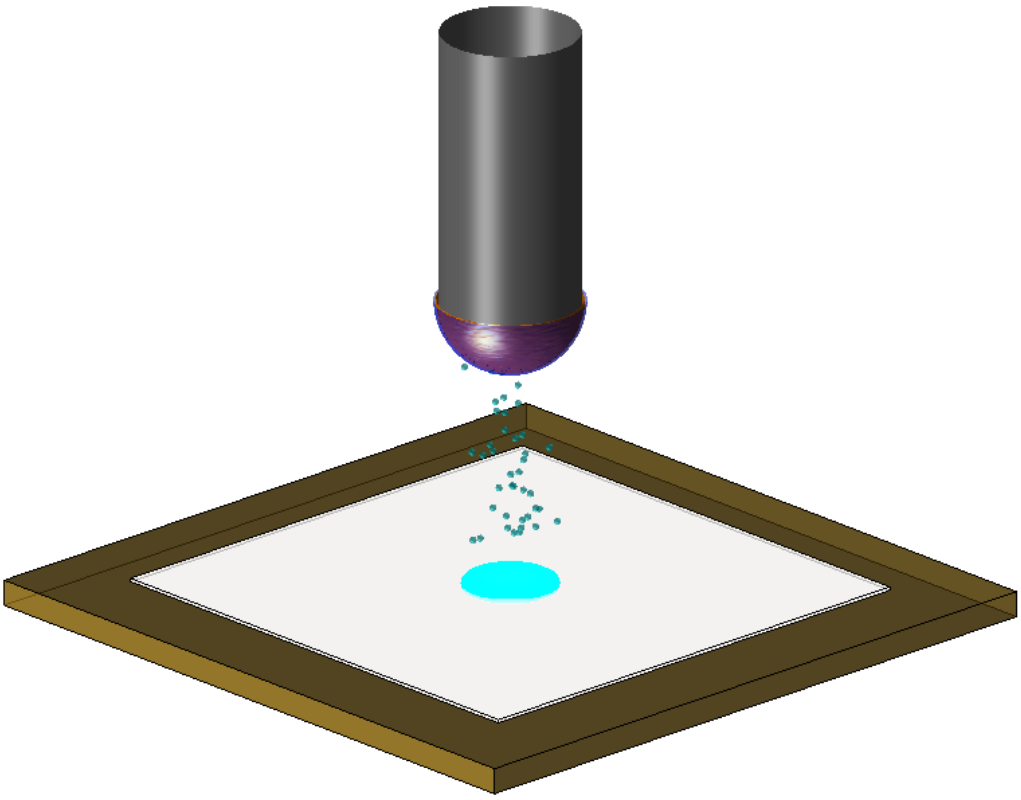

Humidity Dependent Surface Charging In Air For HVDC Applications

Master's thesis in Sustainable Electric Power Engineering and Electromobility

Jin Wang

DEPARTMENT OF ELECTRICAL ENGINEERING

CHALMERS UNIVERSITY OF TECHNOLOGY
Gothenburg, Sweden 2024
www.chalmers.se

Master's thesis 2024

Humidity Dependent Surface Charging In Air For HVDC Applications

Jin Wang

CHALMERS
UNIVERSITY OF TECHNOLOGY

Department of Electrical Engineering
Division of Electric Power Engineering
Chalmers University of Technology
Gothenburg, Sweden 2024

Humidity Dependent Surface Charging In Air For HVDC Applications
Jin Wang

Supervisor: Olof Hjortstam, Hitachi Energy Research
Xiangdong Xu, Chalmers University of Technology
Examiner: Xiangdong Xu, Chalmers University of Technology

Master's Thesis 2024
Department of Electrical Engineering
Division of Electric Power Engineering
Chalmers University of Technology
SE-412 96 Gothenburg
Telephone +46 31 772 1000

Cover: 3D Model of Rod-Plate Electrode Charging Setup in Humid Air

Typeset in LaTeX
Printed by Chalmers Reproservice
Gothenburg, Sweden 2024

Humidity Dependent Surface Charging In Air For HVDC Applications
Jin Wang
Department of Electrical Engineering
Chalmers University of Technology

Abstract

This thesis investigates the dynamic interactions between surface charge generation at electrode-air interface and charge accumulation at dielectric-air interfaces under different atmospheric humidity, crucial for enhancing insulation performance in high-voltage direct current (HVDC) systems. Despite their critical role, the mechanisms of interface charging and the influences of humidity, have been underexplored. Through comprehensive experimental setups and a detailed test matrix, this study systematically explores how varying humidity levels affect surface charge dynamics. Employing a new experimental setup with newly developed humidity control systems, the research offers insights into the charge generation mechanism by investigating the dielectric-air interface charge accumulation dynamics under different stress conditions, providing a foundation for future enhancements in HVDC insulation technology.

Keywords: HVDC insulation, charge generation, charge accumulation, humidity, dielectric-air interfaces, electrical field strength, experimental setup.

Acknowledgements

Firstly, I would like to express my gratitude to my supervisors, Dr.Olof Hjortstam at Hitachi Energy Research and Dr.Xiangdong Xu at Chalmers, for giving me the opportunity to research this fascinating topic. I couldn't have worked efficiently without their support in high-voltage engineering theory and practical experimental work. Their continuous encouragement and recognition over the past few months have been instrumental in helping me overcome a lot of challenges during my thesis work.

Secondly, I would like to thank Daniel Svensson for providing a well-designed prototype of the experimental setup and sharing his valuable experience on this topic. He has always been available for discussions whenever I encountered obstacles, offering both support and understanding. I am equally grateful to Prof.Yuriy Serdyuk for his continuous care and willingness to offer suggestions throughout my research.

Finally, I cannot say enough thanks to my entire family, especially my dear wife and friend, Zhen Zhu, and my daughter, Yibei Wang. Their unconditional love and support have been my pillars, standing by my side throughout this wonderful journey.

Jin Wang, Gothenburg, May 2024

List of Acronyms

Below is the list of acronyms that have been used throughout this thesis listed in alphabetical order:

AH	Absolute Humidity
DC	Direct Current
DAQ	Date Acquisition
$E_{\max}$	Maximum electric field strength
HVDC	High-Voltage Direct Current
PD	Partial Discharge
RH	Relative Humidity
PI	Polyimide
PET	Polyethylene Terephthalate

Contents

List of Figures

List of Tables

1
Introduction

This thesis investigates the effects of humidity on surface charging in air, specifically for High-Voltage Direct Current (HVDC) applications. Building upon D.Svensson's master thesis [1], this research extends the examination of charge generation at electrode-air interface as well as charge accumulation at polymer-air interfaces under direct current (DC) voltage. Unlike previous studies that primarily focused on a static electrical condition, this study broadens the experimental scope to include a variety of conditions. By analyzing the diverse dynamics of charge accumulation, this work aims to enhance our understanding of the fundamental processes behind charge generation in humid air, particularly under stresses below the electron avalanche onset voltage. This chapter outlines the thesis project, detailing the study's background, current challenges, and research objectives and goals.

1.1 Background

HVDC transmission plays a vital role in efficiently transmitting power over long distances, which challenges the insulation system due to the high voltage level. Polymeric materials are essential elements of HVDC insulation systems, owing to their favorable dielectric properties, lightweight design, and corrosion resistance. Materials such as polyethylene, silicone rubber, epoxy resin, and more find application in various roles, including insulators, cable accessories, and bushings. The performance of polymeric insulation holds a critical role in ensuring the safety and stability of HVDC systems. It necessitates robust insulation strength and favorable surface properties to prevent partial discharge or potential breakdown. These performance aspects are particularly sensitive to environmental conditions, especially in outdoor appliances. Environmental factors like temperature and humidity have notable impacts on dielectric performance. Notably, a distinct phenomenon known as surface charge accumulation occurs when DC voltage is applied,which affects the flashover voltage [2]. In practical applications, many polymeric insulations are exposed to the atmosphere, with humidity playing a significant role in influencing surface charging at the air-polymer interfaces.

Recent theses have investigated the effects of humidity, revealing significant findings. In P.Mundim's work [3], it was observed that the current in air under a homogeneous electric field exponentially increases with rising air humidity. Similarly, D.Svensson's study [1] identified an exponential relationship between charge accumulation at the polymer-air interface and air humidity. Additionally, E.Svensson's research [4] explored the formation of water layers on metal surfaces in humid air, which are as-

sociated with charge emissions. Despite these advancements, the charge generation mechanism in the charge accumulation process remains inadequately explored.

1.2 Problem statement

The prior study [1] [5] primarily focused on charge accumulation under static conditions, without providing insights into how dynamic changes in humidity affect charge behavior at polymer-air interfaces. To deepen our understanding of the mechanisms behind charge generation, it is essential to further investigate the interactions between humidity and various factors including electric field stress, electrode surface conditions, and air volume.

1.3 Purpose

The purpose of this study is to investigate how humidity impacts charge accumulation at air-polymer interfaces across various conditions, including voltage, air gap length, electrode radius, and polarity. This detailed exploration aims to enhance our knowledge of the charging dynamics under diverse conditions, providing insight into the charge generation mechanism.

1.4 Research Goals

- Reinstall and upgrade the previous experimental setup [1] to provide varying electrical and humidity conditions, and assess its performance enhancements.
- Select a dielectric material based on both theoretical and experimental analysis.
- Design the experimental procedure and develop a test matrix based on simulations and trial tests.
- Conduct experiments under the designed configurations to analyze the interactions between humidity and surface charge accumulation at polymer-air interfaces, exploring the charge generation mechanisms.

2

Literature review and background study

This chapter presents an overview of the literature relevant to this study. In section 2.1, the mechanism of interface charge accumulation is explained through the introduction of a dielectric-air interface model in a homogeneous electric field, accomplished by deriving the mathematical model of the Maxwell-Wagner capacitor in the time domain. In section 2.2, the effect of humidity is explored with a review of relevant research on the charge generation mechanism in atmospheric air to establish the connection between atmospheric humidity and surface charge accumulation. In section 2.3, the findings from Daniel's [1] and P.Mundim's study [3] are discussed to provide a foundation for this thesis.

2.1 Charge accumulation mechanism

2.1.1 Fundamental theory

- **Conductivity in air**
  According to Townsend's criterion, Figure 2.1 shows the E-I characteristic curve in air under a homogeneous electric field is divided into three stages: the ohmic region, the saturation region, and the avalanche region [6]. Below the inception of corona discharge, the currents in the ohmic and saturation regions are interconnected, indicating the mixed charge generation mechanism.
  The current density in the ohmic region following Ohm's Law [7] ,

$$\vec{J} = \sigma \vec{E} = \rho \mu \vec{E} \tag{2.1}$$

  where $\vec{J}$ is the current density, ρ is the charge density, μ is the charge carrier mobility, and $\vec{E}$ is the electric field vector.
  The conductivity σ is given by:

$$\sigma = \sum_i \rho_i^+ \mu_i^+ + \sum_i \rho_i^- \mu_i^- \tag{2.2}$$

  where:
  - σ is the conductivity,
  - ρ_i^+ and ρ_i^- are the positive and negative charge densities, respectively,
  - μ_i^+ and μ_i^- are the electrical mobilities of the positive and negative charge carriers, respectively.

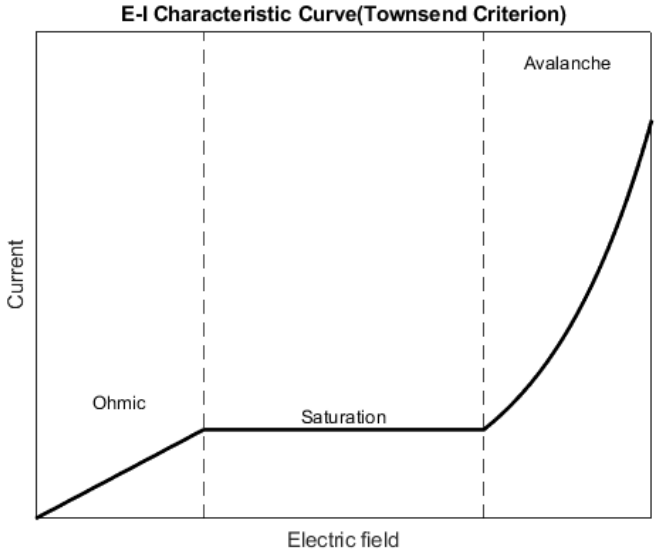

Figure 2.1: E-I characteristic curve in the homogeneous electric field

The characteristics of electrical current are influenced by various factors, including the concentration of charge carriers, their mobility, and their polarity. Importantly, the magnitude of the current is limited by the rate at which these charge carriers are generated.

- **Charge accumulation on the dielectric interface**
  When a dielectric material is subjected to DC voltage, an electric field is created through the combined effects of the displacement field and the conduction field. The displacement field arises from the shift in charge carriers, a process known as polarization. Meanwhile, the conduction field results from the movement of these charge carriers, a phenomenon referred to as conduction. Considering setup with layered dielectric materials, such as an polymer-air arrangement, Gauss's law of continuity delineates the relationship between the displacement current density and the conduction current density.

$$J_{1n} + \frac{\partial D_{1n}}{\partial t} = J_{2n} + \frac{\partial D_{2n}}{\partial t} \tag{2.3}$$

In a steady-state condition under DC voltage application (where dD/dt = 0), the stationary conduction field ensures the continuity of conduction current density at the interface, leading to the balance of current density.

$$J_{n1} = J_{n2} \tag{2.4}$$

However, any variation such as switching, polarity reversal, or changes in magnitude induces a displacement field due to the inherent delay in polarization. This results in a transient process that disrupts the continuity of the conduction current density at the interface. During this phase, the number of charge carriers moving into the interface does not equal the number moving out. Most are left on the dielectric surface, leading to the surface charge accumulation.

2.1.2 Maxwell-Wagner capacitor model

The Maxwell-Wagner effect is utilized to model the accumulation of interface charge in multi-layered dielectrics [6]. This approach is also relevant in our current study, particularly for examining charge dynamics on the dielectric-air interface. Figure 2.2 shows the dielectric-air arrangement model.Figure2.3 depicts the Maxwell-Wagner two-layer capacitor model, which is utilized to express a step-like excitation process immediately after a DC voltage is applied. It can effectively describe the transient behavior of potential variation.

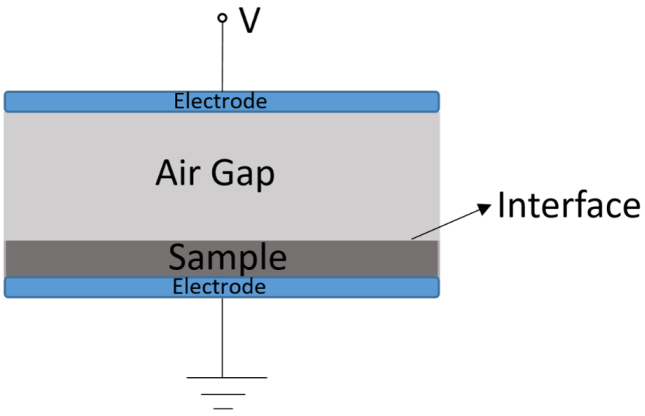

Figure 2.2: dielectric-air interface arrangement model

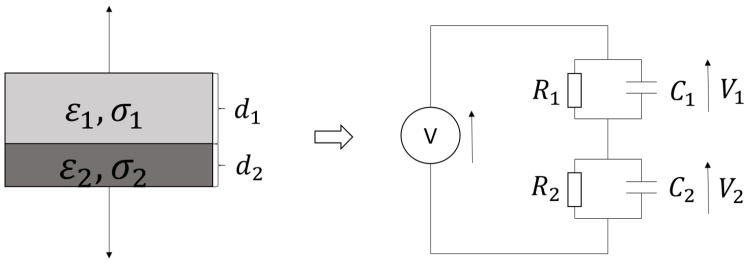

Figure 2.3: Maxwell-Wagner two-layer capacitor model

The total voltage V is the sum of V_1 and V_2. The current I can be expressed in terms of the capacitors and resistors in the circuit as $I = \left(C_1 \cdot \frac{dV_1}{dt} + \frac{V_1}{R_1}\right) = \left(C_2 \cdot \frac{dV_2}{dt} + \frac{V_2}{R_2}\right)$. The capacitances C_1 and C_2 are given by $C_1 = \frac{A\epsilon_1}{d_1}$ and $C_2 = \frac{A\epsilon_2}{d_2}$, respectively, where A is the area of the capacitor plates, ϵ_1 and ϵ_2 are the permittivities, and d_1 and d_2 are the distances between the plates. The resistances R_1 and R_2 are defined as $R_1 = \frac{d_1}{A\sigma_1}$ and $R_2 = \frac{d_2}{A\sigma_2}$, with σ_1 and σ_2 being the conductivities.
Initially, the field distribution follows the geometrical Laplacian field, satisfying $D_1 = D_2$, which implies $\epsilon_1 E_1 = \epsilon_2 E_2$. The final field distribution is determined by the conductivity, leading to $J_1 = J_2$ and consequently $\sigma_1 E_1 = \sigma_2 E_2$. By integrating these equations, the charge density at the interface can be computed as a function of time:

$$\rho(t) = \frac{\epsilon_2\sigma_1 - \epsilon_1\sigma_2}{d_1\sigma_2 + d_2\sigma_1} V(1 - e^{-t/\tau}) \tag{2.5}$$

where

$$\tau = \frac{\epsilon_2 d_1 + \epsilon_1 d_2}{d_1 \sigma_2 + d_2 \sigma_1} \tag{2.6}$$

In the context of the Maxwell-Wagner capacitor model, the accumulation of interface charge is described by an exponential function, assuming that the permittivities ϵ_1, ϵ_2 and conductivities σ_1, σ_2 remain constant.

2.1.3 Surface charge dynamic

When examining the complete dynamics of the charging process, the quantity of interface charge is determined not only by the mechanisms of charge accumulation but also by those of charge decay. The main mechanisms of charge decay include bulk neutralization, surface conduction, and gas neutralization [8]. Bulk neutralization occurs within the material itself due to internal charge conduction, charge injection, and polarization. Surface conduction involves the movement of charge through leakage currents driven by an uneven tangential field along the interface. Gas neutralization is the process by which free air ions attach to the interface, neutralizing the surface charge.
In S.Kumara's study [9], the decay rates of these mechanisms are analyzed. For the material 'powersil', which has a bulk conductivity of $3.5 \times 10^{-15}\, S \cdot \mathrm{m}^{-1}$ and a surface conductivity of $3.3 \times 10^{-14}\, S \cdot \mathrm{m}^{-1}$, it was observed that surface charge decayed from 100% to 50% over 1500 seconds under natural conditions without corona discharge, and approximately 350 seconds with enhanced gas neutralization via corona discharge.
This significant level of charge decay cannot be ignored during the extended charging periods, which last several hours. The charge measured at the interface can not accurately represent the cumulative charge without considering these decay processes. Given the complexity of measuring charge decay, for research that corresponds to charge accumulation through surface charge measurements, choosing materials with low bulk and surface conductivity is beneficial to minimize charge decay effect.

2.2 Humidity effect on charge generation

As described in the previous section, the charge generation in the charge accumulation process is dominated by the free charges from air, which should be several orders of magnitude greater than the induced charges via dielectric bulk,provided that the bulk material exhibits sufficiently low conductivity and negligible charge decay. The air current originates dynamically from electric field stress and the presence of free charges, as outlined in Equations 2.1 and 2.2. Humidity plays a critical role in this dynamic, as explored in E.Svensson's thesis [4].
The air humidity represents the content of water vapor in the moist air, which consists of approximately 78% nitrogen, 21% oxygen, 1% argon, and other minor components. Humidity levels are determined at the dew point, where water vapor saturation occurs, equating the rates of vaporization and condensation. Absolute Humidity (AH) and Relative Humidity (RH) are common metrics for representing these levels [10].

At the air-solid interface, phenomena such as water adsorption and desorption occur, involving both chemical and physical mechanisms [11]. This leads to the natural formation of a water adlayer on the interface, reaching an equilibrium between adsorption and desorption processes. The thickness of this adlayer is influenced by factors including material properties, surface roughness, and humidity levels [12]. When exposed to an electric field, further electrochemical reactions on the water adlayer are investigated in several studies [13] [14] [15], as detailed in an air-electrode interface model, illustrated in Figure 2.4.

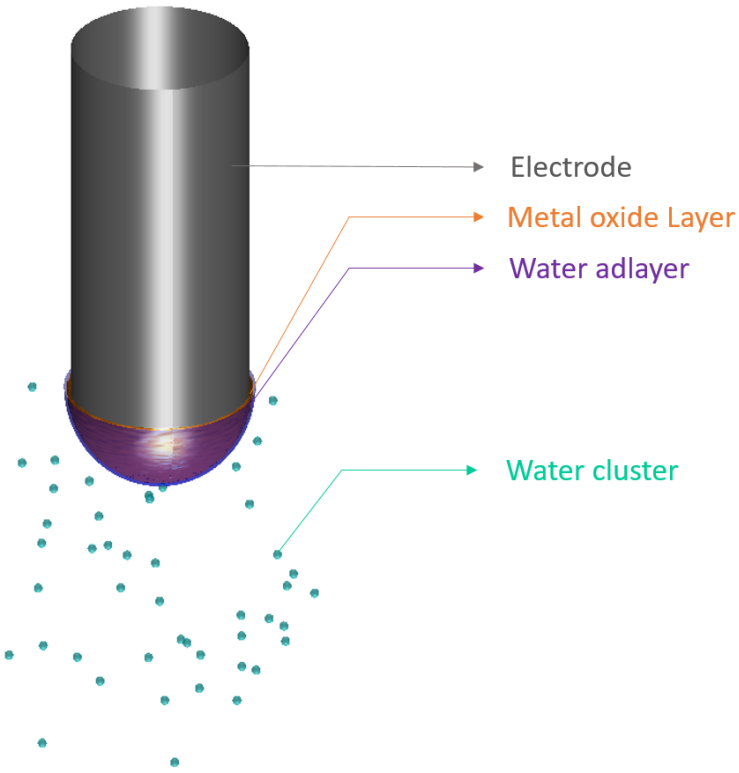

Figure 2.4: Air-electrode interface model for electrochemical reactions

Air-electrode interface model with a rod metal electrode exposed to moist air, applying a positive voltage to create an ambient electric field. In the model, a water adlayer forms outside the metal oxide layer, a common phenomenon on metal surfaces [16].
The overall electrochemical process can be simplified into three steps:

1. Formation of the initial water adlayer through adsorption and desorption [13].
   $H_2O^* \rightleftharpoons H_2O$
2. Dissociation of water molecules into hydroxide and proton ions [14] [15].
   $mH_2O \rightleftharpoons H^+(H_2O)_n + OH^-(H_2O)_{m-n-1}$
3. Driven by the electric field, protons escape from the adlayer, and water molecules in the air gap capture these escaping protons to form positive water cluster. Concurrently, the area from which the protons are emitted experiences an intensified electric field due to negatively charged adlayer, which enhances the dissociation of ions. [14] [15].

$H^+(H_2O)_n \rightarrow H^+(H_2O)^*_{m\leq n} + (n-m)H_2O$

The substances marked with an asterisk (*) are dispersed in the air, while the remaining substances adhere to the surface. For electrodes with a negative voltage, a similar electrochemical process occurs, where heavier hydroxide ions are emitted into the air instead.

The influence of the electric field on these processes is substantial [17]. In E.Svensson's study, the thickness of the water adlayer was indicated to be thinner under a positive electric field compared to neutral conditions, indicating a higher rate of proton escape. Moreover, the difference in adlayer thickness varies with humidity levels. This relationship indicates that air humidity influences the formation of water cluster ions at the electrode-air interface, potentially affecting charge generation as well as the charge accumulation process.

2.3 Experimental setup and charge accumulation modelling

The current study builds upon D.Svensson's [1] and P.Mundim's work [3]. D.Svensson's work involved creating an experimental setup to directly measure surface potential and evaluate surface charge density. His Msc thesis provides a prototype for experimental setup design and offers baseline data for surface charge accumulation,as detailed in Section 2.3.1. Meanwhile, P.Mundim's research measured the current in the air under various electrical fields and moisture levels, leading to the development of several functions that relate air current density to different electrical fields and humidity values. This data, combined with the Maxwell-Wagner capacitor model described in Section 2.1.2, enables the construction of a mathematical model to simulate surface charge accumulation in the air-solid system, illustrated in Section 2.3.2. Additionally, this mathematical approximative model outlines methods for designing the test matrix with extended variables, verifying measurements, and quantifying the analysis.

2.3.1 Design and expansion of the experimental setup

Building upon D.Svensson's research [1], this work expands the scope to include a broader range of application conditions, including alterations in geometry, volume, voltage, and polarity. Experiments are carried out in the same sealed plastic chamber, maintaining the core structure of the previous electrode-air-dielectric arrangement. A DC voltage is applied by connecting the electrode to a high-voltage generator. The non-contact surface potential measurement technique, namely the Kelvin probe method, is used for estimating surface charge density. Probe positioning is achieved through a computer-controlled XY table (Arrick Robotics XY30), facilitating the scanning of surface potential distribution. A data acquisition card is employed to record the analog signal from the Kelvin probe system. The humidity recorder TR-73U continues monitoring the humidity levels within the test chamber. To accommodate varied conditions, both electrical and mechanical modifications are necessary to ensure flexible connections of different electrical parts. Given the

anticipation of conducting a significantly higher number of tests compared to the singular condition of the previous study, an efficient and stable humidity control system is implemented. A numerical analysis is recommended for the diverse phenomena observed under various scenarios.

2.3.2 Charge accumulation modeling under different humidity

A further examination is presented in P.Mundim's work [3], a deeper study was conducted on charge generation resulting from variations in humidity. Drawing on the collected data, an exponential relationship between the current density and the electric field across different humidity levels was observed.
The current density in air, J_{air}, can be expressed as a function of the electric field strength E using the equation:

$$J_{\text{air}} = a \cdot e^{b \cdot E} \tag{2.7}$$

where J_{air} represents the current density in air (A/m^2), E is the electric field strength (V/m), and a, b are coefficients. The coefficients in this equation vary with humidity, which was determined by curve fitting based on the measurement(T=295K) in P.Mundim's work [3]. The $E - J$ characteristic achieved in the study is shown in Figure 2.5.

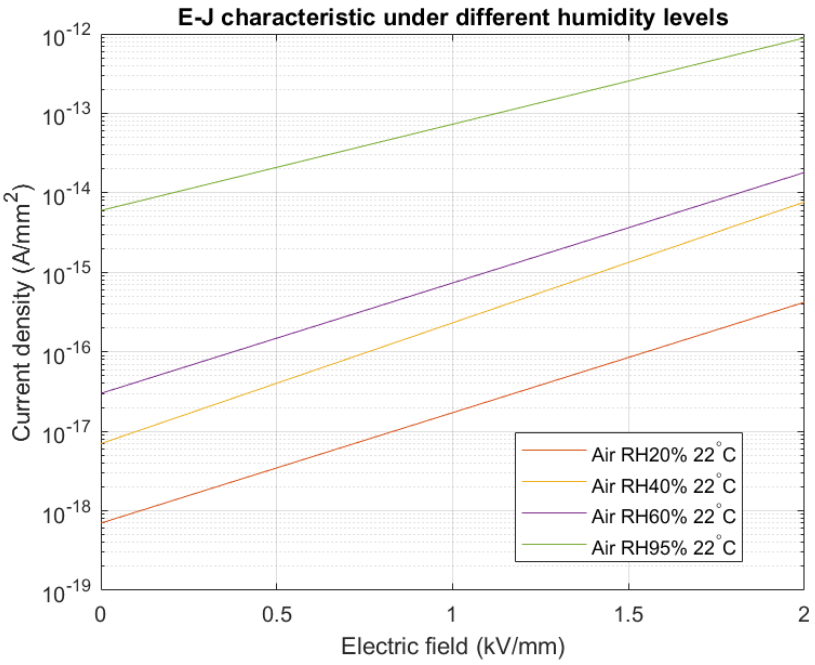

Figure 2.5: E-J characteristic in air from P.Mundim's work.

Derived from the result shown in Figure2.5, the conductivity of air under varying humidity conditions can be represented by the function of the electric field as follows:

$$\sigma_{\text{air}} = \frac{dJ_{\text{air}}}{dE_{\text{air}}} = a \cdot b \cdot e^{b \cdot E} \tag{2.8}$$

Referring to T.Blythe et al.'s book [18], empirical equation 2.9 can be applied to calculate the conductivity of polymeric materials. Taking Teflon, as used in D.Svensson's study [1], as an example – whose conductivity (10^{-20} S/m) [19] is much lower than that of air (10^{-14} S/m) [20] – combined with the results from T.T.N.Vu's study [21], the conductivity of Teflon is considered to be constant at a constant temperature. It also indicates a negligible influence from the electric field, due to its small variation range (< 10 kV/mm). The relation can be described by the following equation:

$$\sigma_{\text{teflon}}(T) = \sigma_0 \cdot \exp\left(-\frac{E_a}{k_B T}\right) \cdot \sinh(\mathrm{B(T)} \cdot \mathrm{E}) \cdot \mathrm{E}^{\alpha} \tag{2.9}$$

where:

- T represents the temperature, set at 295 K, aligning with the testing temperature in P.Mundim's work [3].
- k_B denotes Boltzmann's constant, 8.617×10^{-5} J/K.
- $\sigma_0 = 1 \times 10^{-16}$ S/m.
- E_a represents activation energy, 0.1 J.
- $\sinh(B(T)E)$ and E^{α} are treated as constants when the temperature is held constant and the electric field varies within a small range (< 10 kV/mm).

Referring to the modeling approach demonstrated in T.T.N.Vu's study [21], Gauss's Law is employed in conjunction with the Maxwell-Wagner capacitor model. By incorporating the nonlinear function of air conductivity(Equation 2.8),as derived from P.Mundim's study [3], a set of nonlinear equations is established.

$$\varepsilon_{\text{air}} \cdot E_{\text{air}} = \varepsilon_{\text{teflon}} \cdot E_{\text{teflon}} + \rho(t) \tag{2.10}$$

where

$$\rho(t) = \frac{\varepsilon_{\text{air}} \cdot \sigma_{\text{teflon}} - \varepsilon_{\text{teflon}} \cdot \sigma_{\text{air}}}{d_{\text{air}} \cdot \sigma_{\text{teflon}} + d_{\text{teflon}} \cdot \sigma_{\text{air}}} \cdot V \cdot (1 - e^{-t/\tau}) \tag{2.11}$$

and

$$\tau = \frac{\varepsilon_{\text{air}} \cdot d_{\text{teflon}} + \varepsilon_{\text{teflon}} \cdot d_{\text{air}}}{d_{\text{air}} \cdot \sigma_{\text{teflon}} + d_{\text{teflon}} \cdot \sigma_{\text{air}}} \tag{2.12}$$

This framework adopts a homogeneous bi-dielectric configuration consistent with the parameters outlined in D.Svensson's study [1]. The setup includes a 3 mm air gap coupled with a 0.5 mm Teflon layer, and is subjected to an applied voltage of 4 kV, as depicted in Figure 2.6. This voltage remains below the partial discharge(PD) inception threshold for the air gap, thus ensuring that the maximum electric field in the air does not surpass the 3 kV/mm, PD inception threshold [6]. Based on this configuration, the following boundary conditions and initial values are defined:

$$\text{Boundary condition: } E_{\text{air}} \cdot d_{\text{air}} + E_{\text{teflon}} \cdot d_{\text{teflon}} = V \tag{2.13}$$

$$\text{Initial value: } \varepsilon_{\text{air}} \cdot \varepsilon_0 \cdot E_{\text{air0}} = \varepsilon_{\text{teflon}} \cdot \varepsilon_0 \cdot E_{\text{teflon0}} \tag{2.14}$$

Where the parameters in the equations are defined as follows:

- $\varepsilon_{\text{air}} = 1.0006$, representing the relative permittivity of air.
- $\varepsilon_{\text{teflon}} = 2.1$, representing the relative permittivity of Teflon.

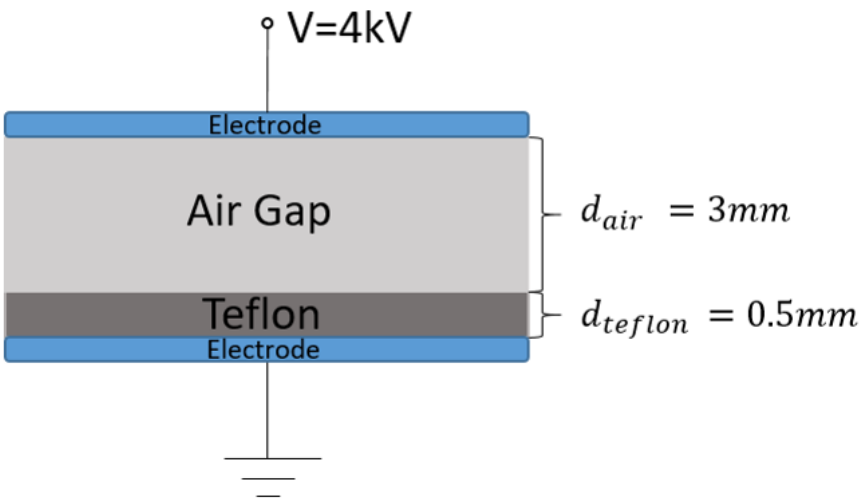

Figure 2.6: Homogeneous bi-dielectric configuration.

- $d_{\text{air}} = 3$ mm, the thickness of the air layer.
- $d_{\text{teflon}} = 0.5$ mm, the thickness of the Teflon layer.
- $V = 4$ kV, the applied voltage across the bi-dielectric arrangement.

These parameters and conditions enable a detailed examination of the electric field distribution and the charge dynamics within the bi-dielectric system.
Iteration is employed to solve the set nonlinear equations, with the iteration ceasing once the time variable reaches 14,400 seconds(4 hours). This approach facilitates the charge accumulation process, which is illustrated in the accompanying Figure 2.7 and 2.8. To parametrize the impact of humidity on the dynamics of charge

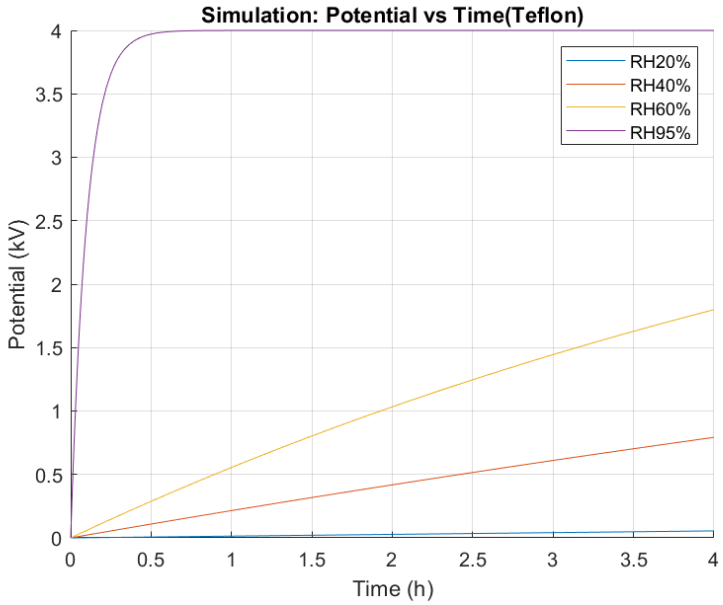

Figure 2.7: Simulation of the surface potential variation.

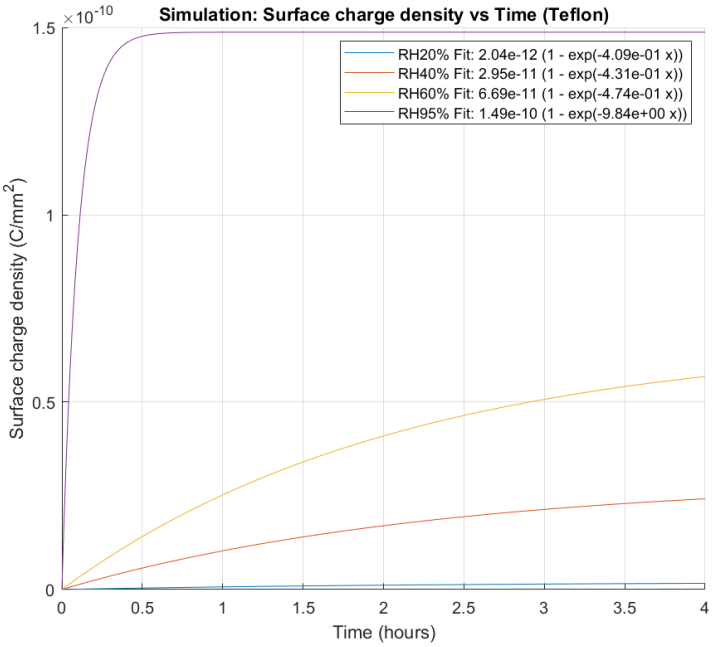

Figure 2.8: Simulation of the surface charge accumulation.

accumulation, exponential fitting was applied to the characteristic curves at various humidity levels. The fitting utilized the function:

$$\rho(t) = a \cdot (1 - e^{-b \cdot t}) \tag{2.15}$$

derived from Equation 2.11. To analyze the charging rate, the first-order derivative of this function was calculated:

$$\frac{d\rho(t)}{dt} = a \cdot b \cdot e^{-b \cdot t} \tag{2.16}$$

The results of these fittings are depicted in Figure 2.8.

Table 2.1: Curve Fit Of Line Charge Density Dynamic For Different Humidity Level.

RH (%)	a	b	$a \cdot b$	Variation Rate: $\frac{a \cdot b(x\%)}{a \cdot b(95\%)}$
20	2.04×10^{-12}	4.09×10^{-1}	8.34×10^{-13}	$5.69 \cdot 10^{-4}$
40	2.95×10^{-11}	4.31×10^{-1}	12.71×10^{-12}	$8.67 \cdot 10^{-3}$
60	6.69×10^{-11}	4.74×10^{-1}	31.71×10^{-12}	0.02
95	1.49×10^{-10}	9.84	14.66×10^{-10}	1.00

As humidity levels increase, the product $(a \cdot b)$ in the first-order derivative functions also increases, indicating a faster initial charging rate. Consequently, this results in more substantial changes of surface charge density at higher humidity levels. By comparing $(a \cdot b)$ variations between 20% RH and 95% RH, as documented in Table

2.1, the intensity of humidity effects can be estimated within this test range. It is important to note that the fitting curves presented in Figure 2.8 are based on measurements of initial electric field strength ranging from 0.5 to 2 kV/mm. This may introduce analysis inaccuracies at very high humidity levels, such as RH95%, where the electric field strength quickly falls below 0.5 kV/mm. Nonetheless, this does not significantly impact the demonstration of the overall trend.
The aforementioned analysis extends from data on ion current in the air, as explored in P.Mundim's work [3], elucidating the effect of humidity on charge dynamics. It confirms findings from D.Svensson's study [1], where charge density at the polymer-air interface, as a function of time, was directly measured under a constant electric field and varying humidity levels. It should be noted that the Maxwell-Wagner model is most suitable for use in a homogeneous electric field arrangement. P.Mundim's study was conducted using a parallel-plate electrode setup with a homogeneous electrical field, whereas D.Svensson's test setup was a rod-plate electrode, which generates an in-homogeneous electrical field. As a result, the simulation outcomes from these studies are rough estimates. However, they provide valuable insights into general trends rather than absolute levels.

3
Experimental procedure

This chapter outlines the methods employed to achieve the objectives of the thesis. Initially, modifications to the existing experimental setup [1] are discussed, focusing on hardware adjustments. Subsequently, a software solution is proposed to enhance the positioning and measurement systems. This is followed by a detailed description of the methodology for selecting dielectric samples. Next, the design of the humidity control system is presented, along with the results of its testing. A test matrix is then designed to guide the experimental process. Finally, determinations of inception voltage for various configurations, as described in the test matrix, are performed using Comsol Multiphysics.

3.1 Experimental setup

As illustrated in Figure 3.1, the experimental setup comprises the following components: a test chamber, a humidity control system, a positioning and DAQ (Data Acquisition) system, and a DC generator along with an electrostatic meter. The test chamber, based on the design described in D.Svensson's study [1], includes a sealed environment, a horizontal support stick, a vertical electrode, a polymeric plate, and calibration and grounding systems. The humidity control chamber is designed to maintain a stable humidity level, as regulated by the system detailed in Section 3.1.2. The horizontal support facilitates the assembly of the electrode and the Kelvin probe, allowing transitions between electrode charging and probe scanning via its connection to the positioning robot. Both the polymeric plate and calibration chop, made from copper, are connected to the same ground to ensure a zero potential state.

3.1.1 Test chamber

The test chamber in D.Svensson's study is utilized with necessary modifications to meet the condition controls required for this study. Figure 3.2 shows that larger grading rings were incorporated at both the junction of the electrode and the horizontal support stick, and the upper edge of the electrode rod. This modification aims to mitigate the risk of partial discharge, a concern due to the application of higher voltages than those used in previous studies. The grading ring's hollow design beneath the horizontal support stick provides the necessary space to accommodate an electrode terminal with adjustable height, thereby allowing for the modification of the air gap length. Furthermore, the electrode height's adjustability is facilitated

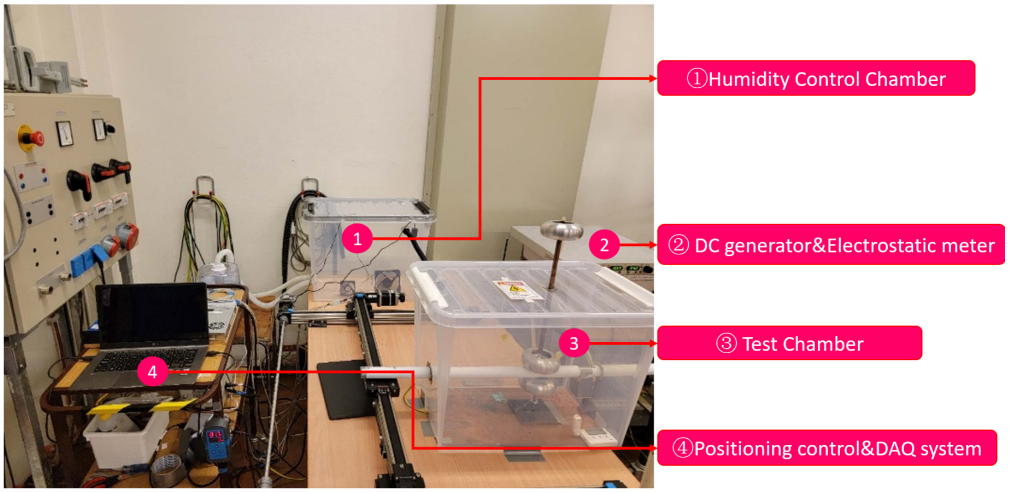

Figure 3.1: Overview of the experimental set-up

by a thread structure. Finally, the air gap length is precisely measured using a series of standardized Mitutoyo® gauge blocks(2mm/3mm/4mm), serving as a reference for adjusting the electrode height, as shown in Figure 3.3.

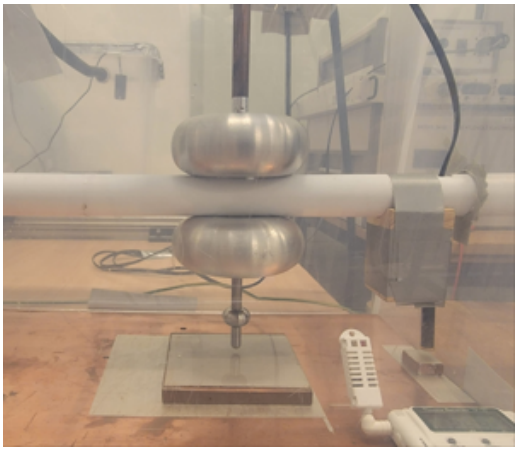

Figure 3.2: Grading Rings

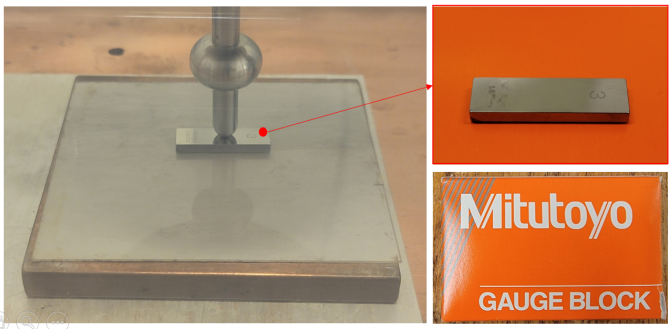

Figure 3.3: Mitutoyo® Gauge Block for adjusting air gap length(3mm)

3.1.2 Humidity control system

Both L.Greenspan [22] and D.Svensson [1] employ binary saturated aqueous solutions to establish fixed air humidity levels. However, tests revealed that achieving steady-state relative humidity with different saturated salt solutions required over minimal two hours, with minor fluctuations arising from chamber leaks and temperature changes. Given the need for a substantial number of tests due to the study's multi-condition environment, there's a need for a more efficient and dynamic humidity control method to increase the efficiency and mitigate the impacts of air leakage and temperature variations.
Building upon F. Küchler's project [23], which introduced a humidity control model, our study has implemented a similar system, as shown in Figure 3.4. This system is modeled after Küchler's design and includes four main components: a humidifier, a dehumidifier, a mixing chamber, and a commercial greenhouse humidity controller. The controller enables the setting of target humidity levels and control margins through an integrated system, featuring two output sockets for powering the humidification and dehumidification devices independently. It activates the humidifier when the humidity exceeds the target plus the margin, and similarly activates the dehumidifier when below this threshold. The humidifier uses an ultrasonic nebulizer with de-ionized water, and the dehumidifier functions by circulating ambient air through silica gel. The mixing chamber ensures uniform distribution of air at the set humidity level within the testing chamber, where the controller's sensor is strategically placed for stable humidity regulation.

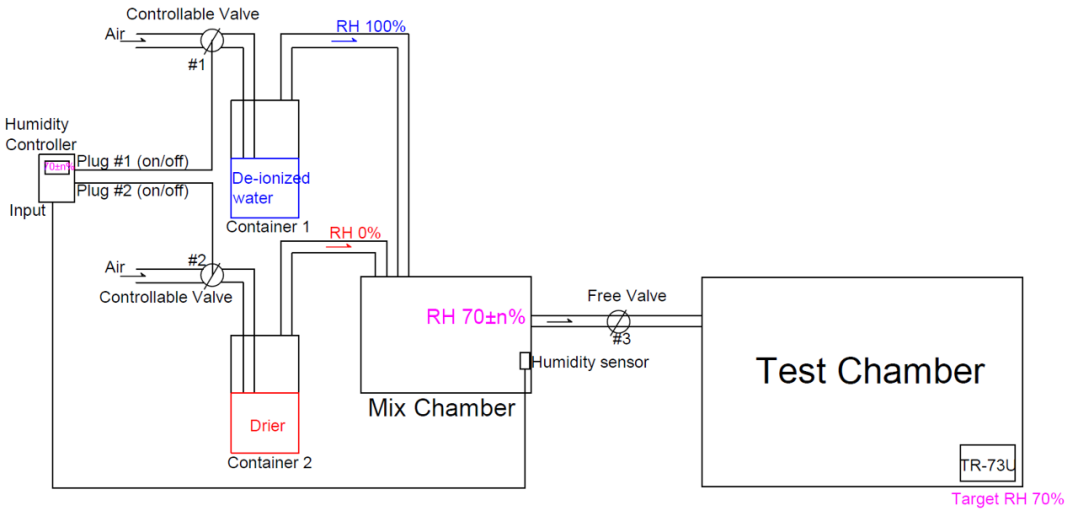

Figure 3.4: Prototype design of the humidity control system

- **System structure simplification and verification**
  The design of our humidity control system is inspired by the prototype in F. Küchler's study [23], but it incorporates self-designed components. To assess its viability and explore potential simplifications, both analytical evaluations and trial tests have been conducted.
  The ambient RH (relative humidity) value in the lab has been recorded, vary-

ing between 20% and 30%. As an extension of D.Svensson's study [1], the experimental RH range is intended to be from 40% to 98%. Accordingly, the dehumidifier has been replaced by directly ventilating ambient air into the system, eliminating the need for a drier container. Additionally, a commercial ultrasonic nebulizer using de-ionized water has been used for humidification.
The necessity of the mixing chamber is confirmed through comparative testing with a target relative humidity (RH) of 60%. Figures 3.6 and Figure 3.7 illustrate these findings. In tests that use the mixing chamber, the RH value remains stable at steady state. Conversely, in tests where the controller's sensor is placed directly in the test chamber without a mixing chamber, the RH value shows fluctuations around the target. Thus, the mixing chamber functions effectively as a buffer for enhancing the stability of the humidity control system.
Based on the simplifications and verifications discussed above, the humidity control system used in this study is illustrated in Figure 3.5.

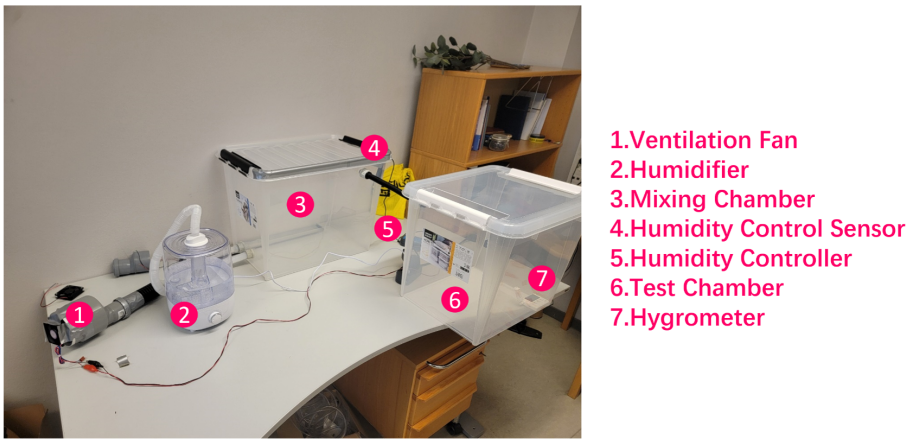

Figure 3.5: Overview of the humidity control system

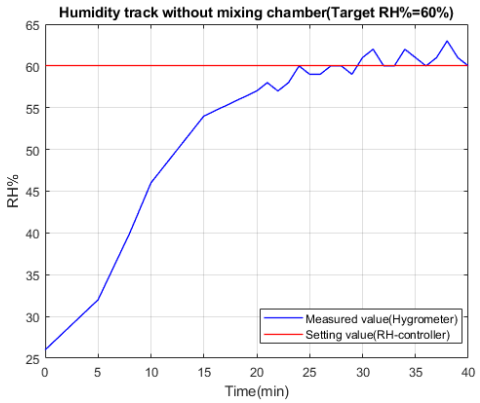

Figure 3.6: Humidity track without mixing chamber

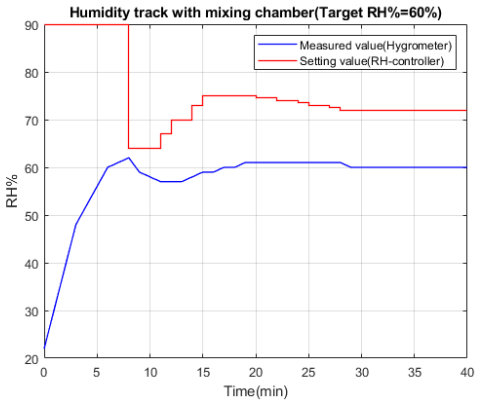

Figure 3.7: Humidity track with mixing chamber

- **System performance evaluation**

To assess the performance of our humidity control system and the relationship between the controller's presets and the actual humidity levels in the test chamber, we conducted a series of tests across different humidity targets. The control strategy began with accelerated humidification, followed by finer adjustment to achieve the target humidity during quasi-steady state conditions. The results, depicted in Figures 3.8 through 3.12 and summarized in Table 3.1, confirm the system's proficiency in maintaining set humidity levels. These findings also guide the user manual for the newly developed equipment. We recommend a higher preset value on the controller to compensate for leakage and sensor discrepancies, especially between the controller's sensor and the TR73 hygrometer. Furthermore, dynamic adjustments to the presets were instrumental in mitigating minor fluctuations that occurred during the intervals of probe scanning.

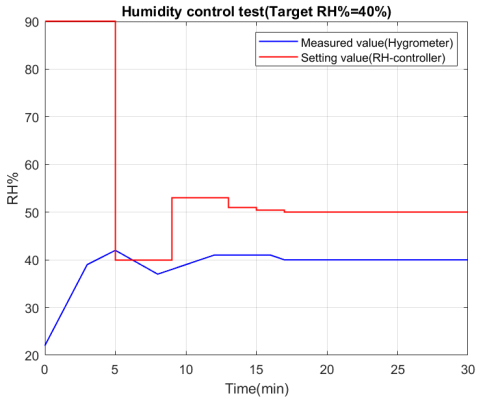

Figure 3.8: Humidity track with target RH value of 40%

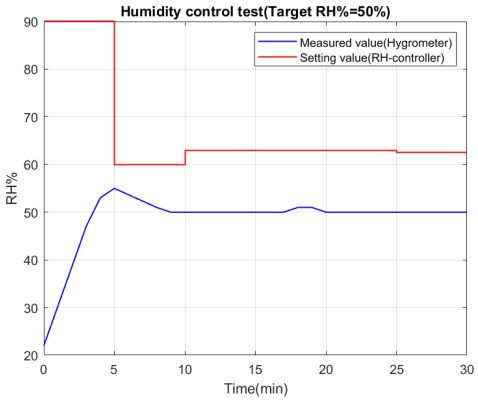

Figure 3.9: Humidity track with target RH value of 50%

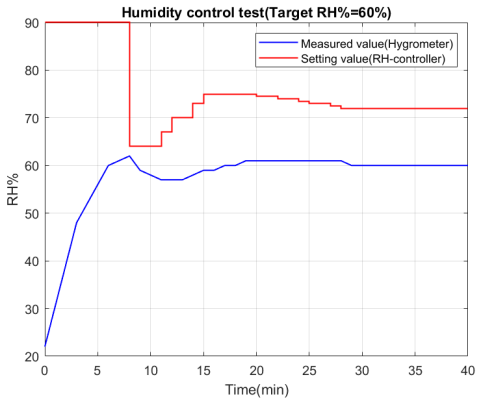

Figure 3.10: Humidity track with target RH value of 60%

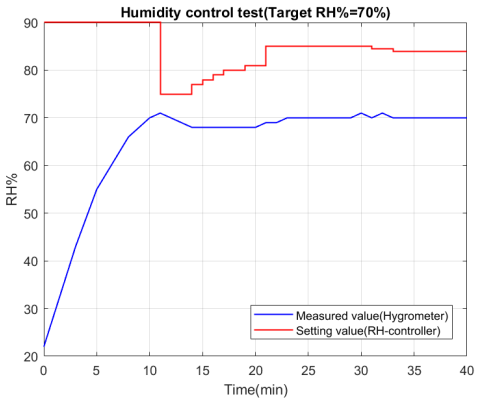

Figure 3.11: Humidity track with target RH value of 70%

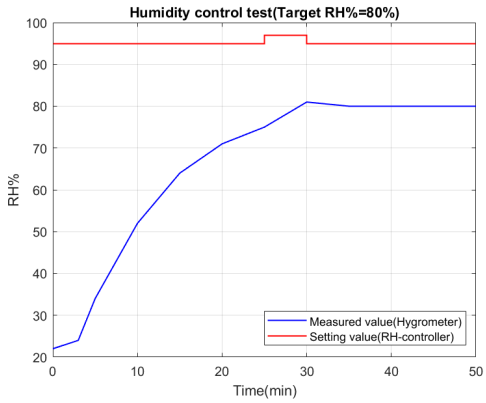

Figure 3.12: Humidity track with target RH value of 80%

Target Humidity	Initial set (%)	Final set (%)	Time (min)
40%	90	51	16
50%	90	62	25
60%	90	73	27
70%	90	84	35
80%	95	95	38
>80%	Manual	Manual	-

Table 3.1: Reference of the humidity control system

3.2 Testing matrix

The purpose of this study is to explore the charge generation mechanism by systematically investigating the effect of humidity on charge accumulation dynamics at the polymer-air interface under various configurations. Humidity serves as the independent variable, while charge density at a specific moment acts as the dependent variable. Other factors, such as voltage, air gap length, electrode radius, and polarity, play varying roles in different configurations, influencing the relationship between humidity and charge dynamics to differing extents.
To streamline this investigation, the mathematical method outlined in Section 2.3.2 is employed to assess the significance of effects by comparing the coefficients derived from polynomial fits to the charge accumulation curves. For instance, the second-order coefficients reveal the non-linearities of these relationships, while the first-order coefficients are indicative of the initial charging rates. These factors facilitate the categorization of tests into different test groups.
Figure 3.13 shows a testing matrix based on the analysis presented. Each column within this matrix represents a unique configuration, with parameters detailed in Table 3.2. This matrix systematically organizes the test framework, facilitating a structured examination of humidity's influence on charge dynamics.

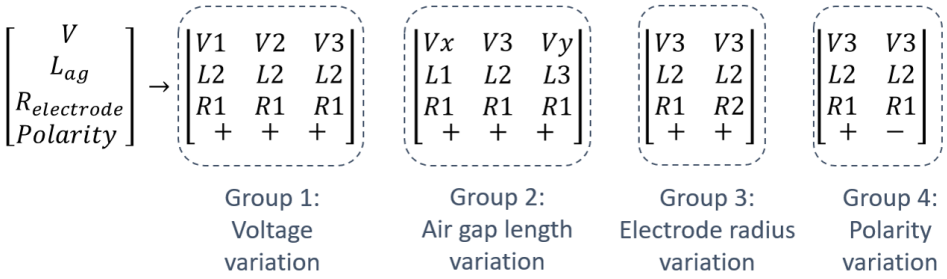

Figure 3.13: Test Matrix

Table 3.2: Parameters in Test Matrix

Factor	**Parameter**	**Value**
Voltage	V1	1 kV
	V2	2 kV
	V3	4 kV
	Vx*	3.1 kV
	Vy*	4.8 kV
Air gap length	L1	2 mm
	L2	3 mm
	L3	4 mm
Electrode radius	R1	4 mm
	R2	7 mm
Polarity	+/-	

*Vx and Vy represent the voltages applied in the 'Air gap length variation' group, adjusted to accommodate variations in air gap length while maintaining a constant maximum electric field at the electrode tip. These values, derived from simulations conducted in COMSOL Multiphysics, are detailed in Section 3.3.

The test matrix is structured into four distinct groups, namely 'Voltage variation', 'Air gap length variation', 'Electrode radius variation', and 'Polarity variation' group. Within the 'Voltage variation' group, different voltages are administered to induce various maximum initial electric field stress($E_{\max}$) at the electrode tip, while maintaining all other factors constant. For the 'Air gap length variation' group, air gap lengths are modified, creating distinct volumes, and voltages are adjusted accordingly to sustain a constant initial $E_{\max}$. The 'Electrode radius variation' group involves testing electrodes of differing radii, introducing variations in both $E_{\max}$ and volume. In the 'Polarity variation' group, the sole variable altered is the polarity of the applied voltage.

This matrix design, coupled with the mathematical model described earlier, positions each column as a discrete test unit. Across these units, a sequence of charge accumulation dynamics is documented within the predefined humidity range for testing. The findings from each group are then cross-compared to understand the effects observed. The column configured with 'V3, L2, R1, +' has been designated as the

reference configuration, replicating the parameters used in D.Svensson's study [1].

3.3 Electrostatic field simulation

To examine the dynamics of charge accumulation in the absence of PD, the test voltages are carefully regulated to maintain the maximum initial electric field ($E_{\max}$) at the electrode below the PD inception threshold of 2.5 kV/mm, as documented in A.Küchler's book [6]. The electrostatic field solutions provided by COMSOL Multiphysics software, following the methodology outlined in D.Svensson's study [1], are employed in configurations requiring $E_{\max}$ calculation.
In accordance with the test matrix detailed in Section 3.2, for the 'Voltage variation' group, it is essential to validate $E_{\max}$ under the reference configuration, which utilizes the highest test voltage. In the 'Air gap length variation' group, the voltages Vx and Vy are determined by calibrating them to produce an $E_{\max}$ equivalent to that in the reference configuration. Simulations for the 'Electrode radius variation' and 'Polarity variation' groups are not necessary, as the $E_{\max}$ values in these configurations are theoretically not exceeding those of the reference configuration.

- **Model implementation**
  The model was developed using the electrostatics module in Comsol Multiphysics, chosen for its ability to accurately simulate the initial Laplacian electrical field where $E_{\max}$ occurs [6]. A 2D model was implemented to represent the object geometry, as shown in Figure 3.14. This approach allows for reduced complexity and increased computing efficiency. As boundary conditions, the ground potential is set to zero, while the electrode potential and the air gap length are adjusted based on various configurations.

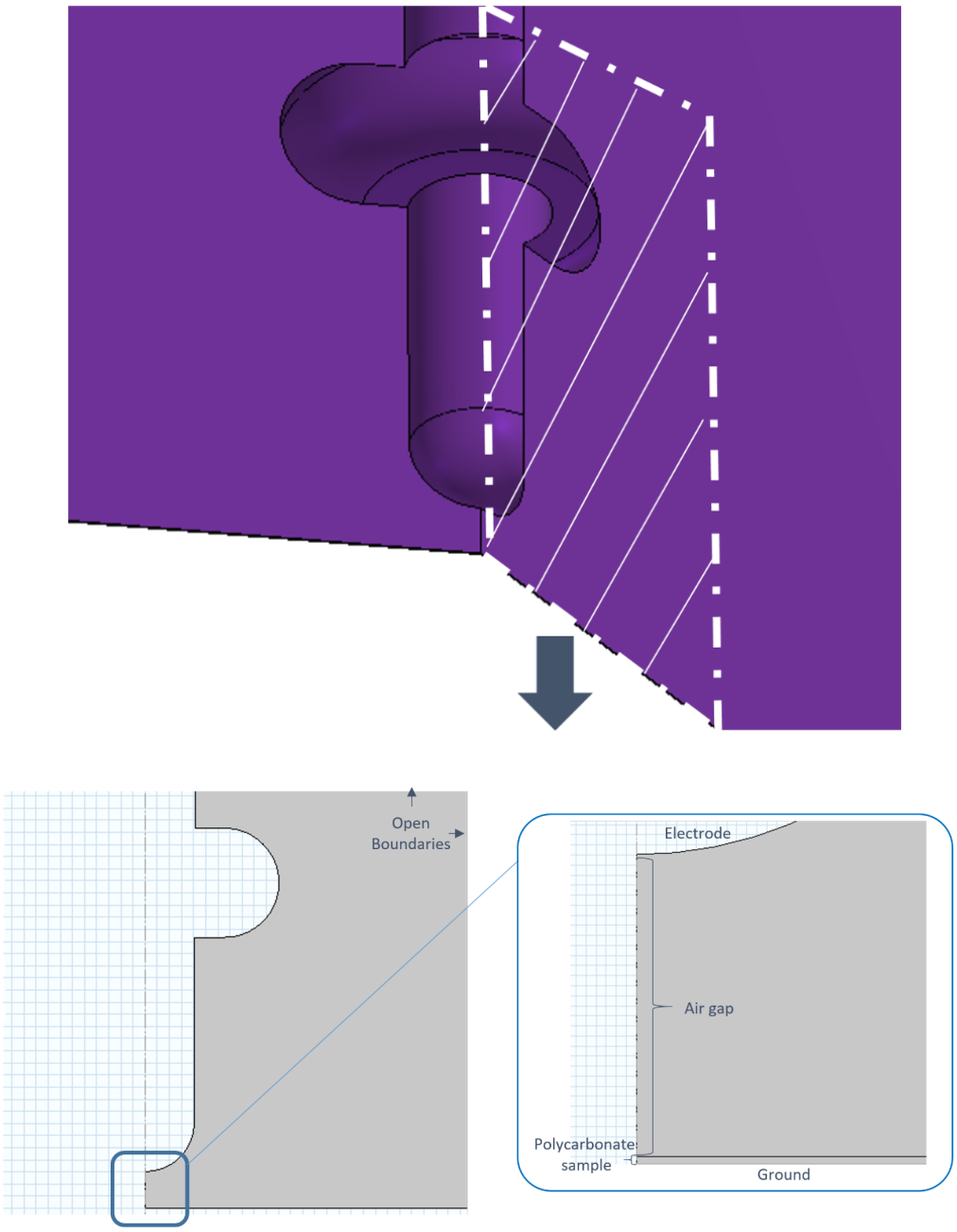

Figure 3.14: The Computational Model Geometry in Comsol Physics

- **E_{max} validation in the 'Voltage variation' group**
  The simulation utilized a configuration with a 3 mm air gap and an electrode potential of 4 kV. Based on Gauss' Law and the definition of potential difference, the maximum electric field strength is observed at the electrode tip. A line potential distribution from the sample surface to the electrode tip was plotted, and the results are presented in Figures 3.15 and 3.16. The calculated E_{max} is 2.05 kV/mm, which remains well below the threshold for partial discharge.
- **Vx and Vy calculation in the 'Air gap length variation' group**

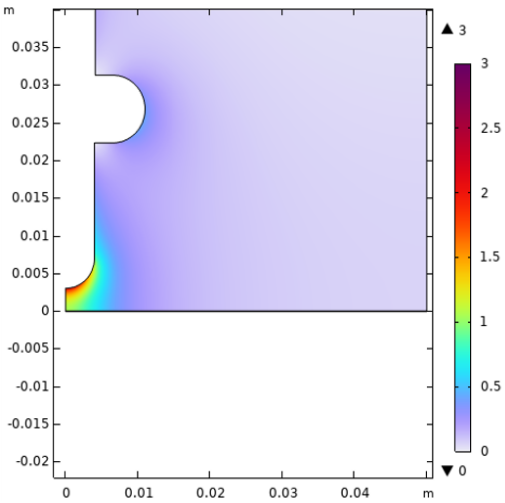

Figure 3.15: Electrical Field Distribution In 2D Model(Configuration:V3=4kV,L2=3mm, R1=4mm,Positive polarity)

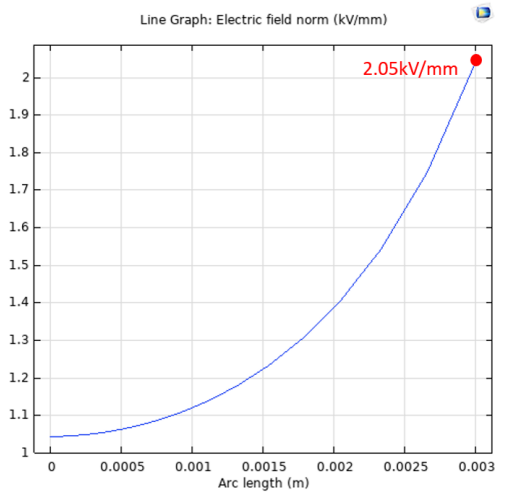

Figure 3.16: Electrical Field Distribution Along The Vertical Axis From The Sample Surface To The Electrode Tip(Configuration:V3=4kV,L2=3mm, R1=4mm,Positive polarity)

In the 'Air gap length variation' group, configurations with varying air gap lengths are employed. To maintain consistency across tests, a constant $E_{\max}$ of 2.05 kV/mm, validated in the base configuration, is used to determine the applied voltages for specific air gap lengths. Given the size constraints of the existing test chamber, comparative air gap lengths of 2 mm and 4 mm, both above and below the base value of 3 mm, are selected. Consequently, similar simulations are conducted with adjusted models. Additionally, sweeps of the electrode potential are performed, during which the electric field strength at the electrode tip, $E_{\max}$, is plotted. The resulting voltage values, Vx and Vy, are displayed in Figure 3.17, 3.19, 3.18, and 3.20.

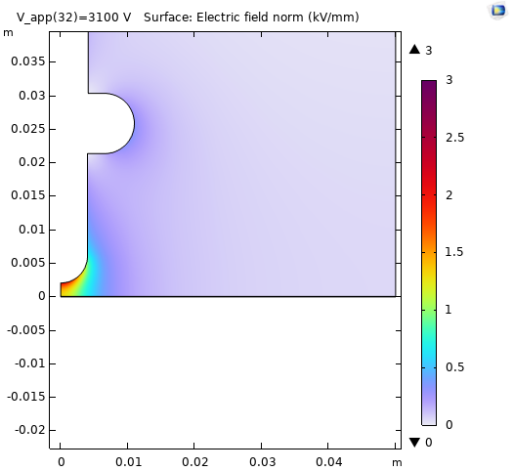

Figure 3.17: Electrical Field Distribution In 2D Model(Configuration:Vx=3.1kV,L1=2mm, R1=4mm,Positive polarity)

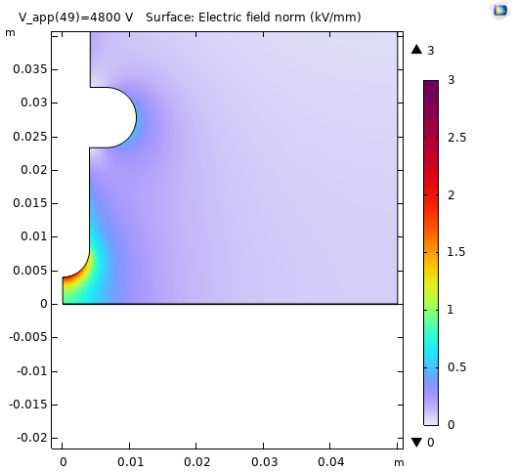

Figure 3.18: Electrical Field Distribution In 2D Model(Configuration:Vy=4.8kV,L2=4mm, R1=4mm,Positive polarity)

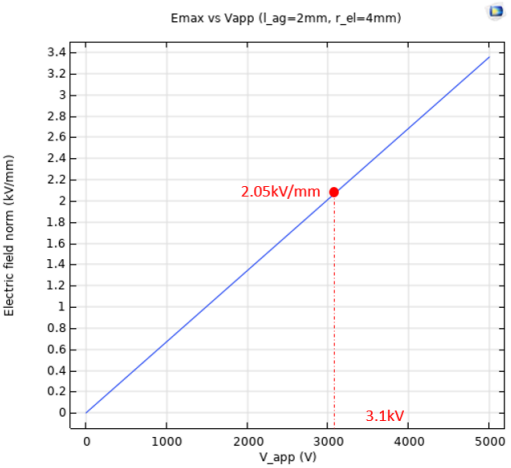

Figure 3.19: Electrical Field Distribution Along The Vertical Axis From The Sample Surface To The Electrode Tip(Configuration:Vx=3.1kV,L1=2mm, R1=4mm,Positive polarity)

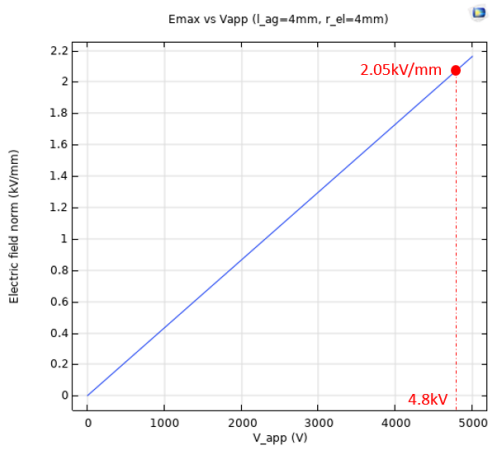

Figure 3.20: Electrical Field Distribution Along The Vertical Axis From The Sample Surface To The Electrode Tip(Configuration:Vy=4.8kV,L2=4mm, R1=4mm,Positive polarity)

3.4 Dielectric material selection

Referring to equations 2.11 and 2.12 derived from the Maxwell-Wagner capacitor model, the conductivity, permittivity, and thickness of the dielectric are the fixed parameters that impact the measurement and analysis of charge accumulation once the experimental sample has been chosen. To simplify the study, it is advisable to neglect the surface charge decay phenomenon by using a sample with sufficiently low conductivity. In this context, Simulations and several trial tests have been conducted with different materials and varying material parameters, aiming to identify the most

suitable material.

- Simulation
  By implementing the mathematical model developed in Section 2.3.2, simulations have been conducted at a fixed RH value of 60% to examine the variations in surface potential over time, with adjustments made to sample parameters. These simulations aim to discern the significance of these parameters on the dynamics of charge accumulation. Given the constraints of the air gap length above the test plate and the materials available in the laboratory, the simulations varied conductivity ($\sigma_0 : 1 \times 10^{-14}$ to 1×10^{-16} S/m), relative permittivity (2.0 to 3.0), and thickness (0.1 to 1.0 mm) of the samples. The results, depicted in Figures 3.21, 3.22, and 3.23, reveal that both conductivity and permittivity are inversely related to the rate of potential variation. Conversely, the rate of potential variation increases with sample thickness. Within the ranges tested, it is evident that sample thickness has a more pronounced impact on the variations in surface potential.

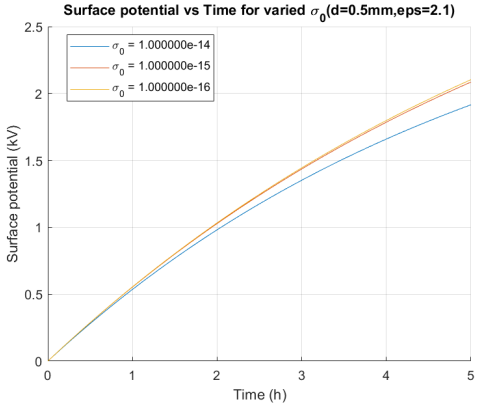

Figure 3.21: Surface potential variations over time for samples with different conductivity

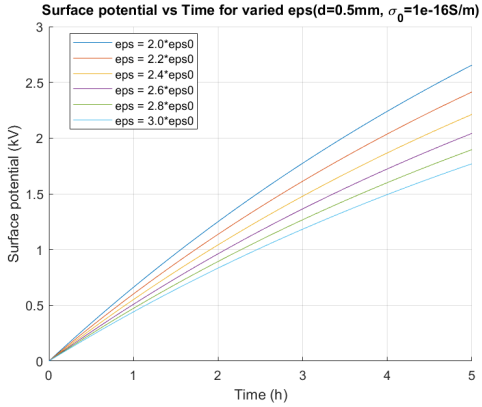

Figure 3.22: Surface potential variations over time for samples with different permittivity

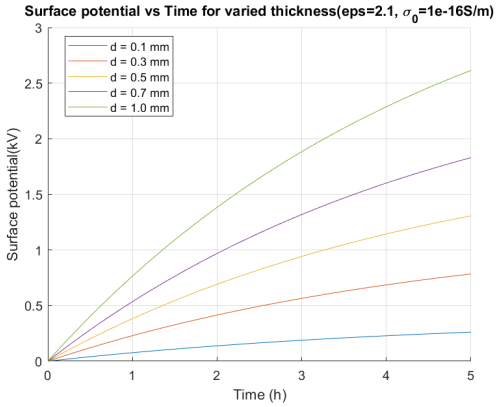

Figure 3.23: Surface potential variations over time for samples with different thickness

Ideally, the goal is to encompass as much of the charging process as possible

within a limited measurement timeframe, achieving a significant variation in surface potential. Per equation 2.6, higher conductivity could shorten the time constant of the charge accumulation process but complicates the analysis due to the introduction of a significant charge decay mechanism, which is deemed unacceptable for this study. As a compromise, materials with lower conductivity are selected, focusing measurements on the early stages of the charge accumulation process(the first hour). This approach is justified since charge accumulation is initially dominated by a much faster charging rate and significantly slows down after several hours. Regarding sample thickness, an appropriately high value is chosen, considering the dimensions of the setup. It is preferable for the sample permittivity to be low; however, this factor may be considered less critical when options are limited.

- Material comparison
  Based on the simulation results, three different samples, as depicted in Figures 3.24 through 3.26, were compared and analyzed.

Figure 3.24: Polymeric films(10-100µm)

Figure 3.25: Telfon roll(1mm)

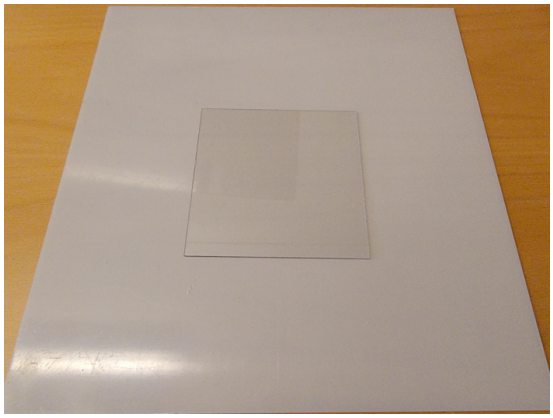

Figure 3.26: Polycarbonate sheet(0.75mm)

The polymeric film, depicted in Figure 3.24, is available in several material options including PI(Polyimide), PET(Polyethylene Terephthalate), and PET-Mica-PET. These materials exhibit a relative permittivity range from 2.1 to

3.4 and a conductivity range from 10^{-14} to 10^{-16} S/m. Additionally, the film samples feature conductive adhesive on their backsides to improve surface contact. However, the inherently thin thickness—below 100 µm—leads to unavoidably low potential variations.
The Teflon sample, illustrated in Figure 3.25, features beneficial properties with a low conductivity of 2×10^{-16} S/m, a relative permittivity of 2.1, and a thickness of 0.95 mm. Nevertheless, the curved nature of the sample complicates placement on the test platform, potentially leading to measurement inaccuracies due to surface contact issues.
The polycarbonate plate, depicted in Figure 3.26, has a conductivity of 5×10^{-15} S/m, a relative permittivity of 2.9, and a thickness of 0.75 mm, which are comparatively less favorable than those of the Teflon sample. However, the impact of these differences is minimal, as confirmed by the simulations. The flat surface of the polycarbonate plate makes it ideally suited for use on the test platform.

3.5 Trial tests

To assess the overall performance of the experimental setup and identify optimal conditions, a number of trial tests were conducted. This section first presents and analyzes preliminary results, including instances of failure, and subsequently proposes an operational process based on empirical findings.
The tests were conducted under 'Reference group' configuration detailed in Section 3.3, at a fixed humidity level. According to the humidity control system's user manual, the theoretical range of humidity control extends from ambient atmospheric levels (approximately 20% RH) to 100% RH. Building on findings from D.Svensson's study [1], which suggest that charging rates increase with humidity, a high humidity level of 98% RH was selected to observe more pronounced charging effects within shorter test durations.
As outlined in Section 3.1.2 and Table 3.1, achieving the target humidity of 98% RH required manual adjustments—specifically, turning off the dehumidifier and manually toggling the humidifier around the target humidity. Following this setup, several 15-minute test groups were conducted, each with different procedures, and the results are discussed below.
In the first experimental group, charging began immediately upon reaching the target humidity; however, no charging was detected on the sample surface, as illustrated by the blue curve in Figure 3.27. Subsequently, after inducing partial discharges by appling a negative voltage of 10kV in the volume on one side of the sample, the electrode was repositioned to charge the sample. This change resulted in significant potential variations on the sample surface, characterized by a strong asymmetrical distribution, depicted by the red curve in Figure 3.27. In the second group, similarly, charging was initiated upon reaching the target humidity with no initial charging detected on the sample surface, as indicated by the blue curve in Figure 3.28. Following this, the electrode surface was cleaned with dust-free paper prior to charging, which uncovered potential variations around the electrode tip, shown by the red curve in Figure 3.28.

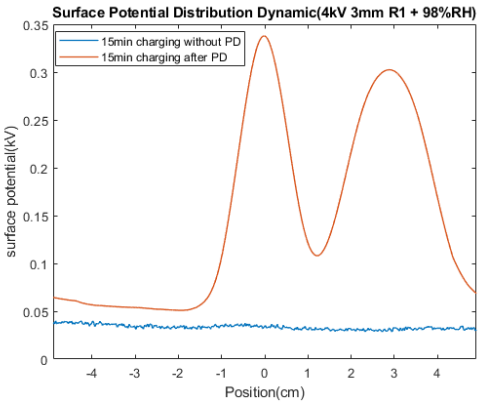

Figure 3.27: Comparison Group 1: 15-minute charging tests at 98% RH before and after creating partial discharge on one side of the sample

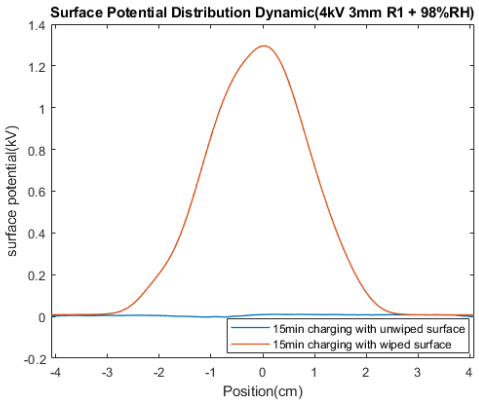

Figure 3.28: Comparison Group 2:15-minute charging tests at 98% RH before and after wiping electrode surface

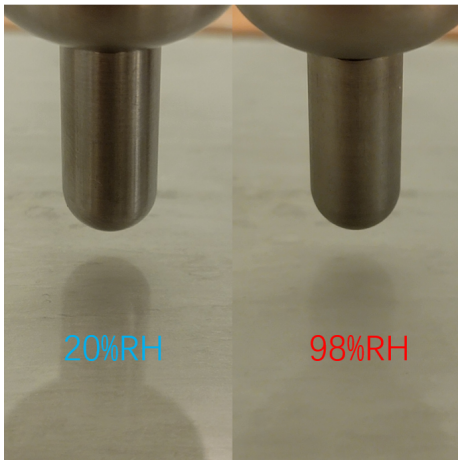

Figure 3.29: Electrode Surface Conditions without condensation at 20% RH and with condensation at 98% RH

These tests confirm the functionality of the improved electrode structure, although achieving a humidity level of 98% RH with the current system is not recommended. The first group's lack of detectable charging is hypothesized to be due to condensation on the electrode surface, as observed in Figure 3.29. The updated humidity control system enhances the efficiency of humidity adjustments but may exacerbate condensation on the electrode surface, potentially masking the charging process. This inference is supported by the significant potential variations observed following the additional partial discharge and cleaning operations, which respectively introduce additional charges into the volume and reduce surface condensation.

Based on the analysis presented above, the surface condition of the electrode is tested to have critical influence the charging phenomenon in the experimental setup. To ensure measurements are comparable across different test groups, maintaining consistent surface conditions is crucial. Accordingly, a detailed investigation into the preconditioning of the electrode surface was conducted under the 'Reference group'

configuration at a RH level of 70%. Initially, the electrode surface was cleaned with isopropanol and placed into the test chamber set to the designated humidity level. The electrode was then subjected to this fixed humidity environment, during which a series of 15-minute charging operations were performed at specific intervals. The results of these operations are documented in Figures 3.30,3.31 and 3.32.

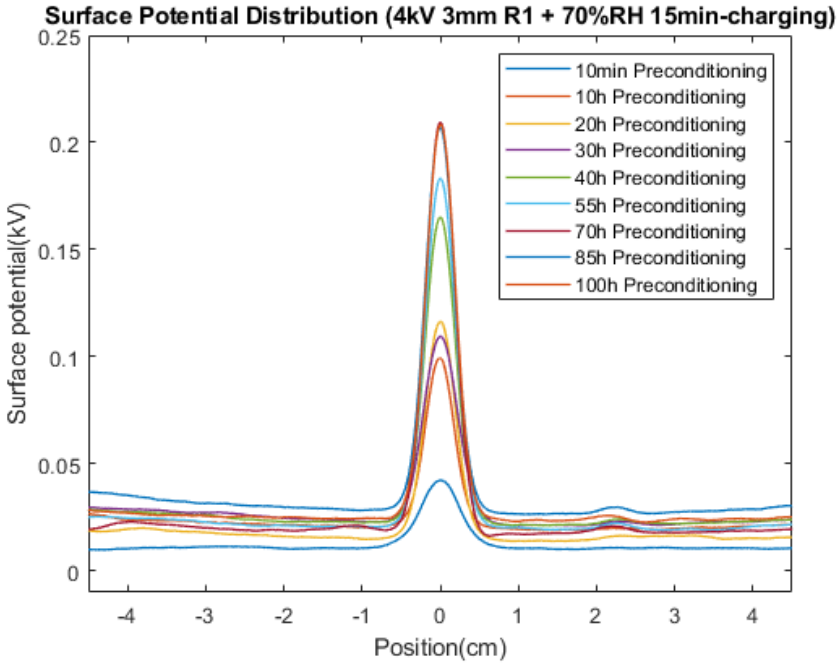

Figure 3.30: Surface Potential Distribution After a 15-Minute Charging Period Following Various Preconditioning Durations

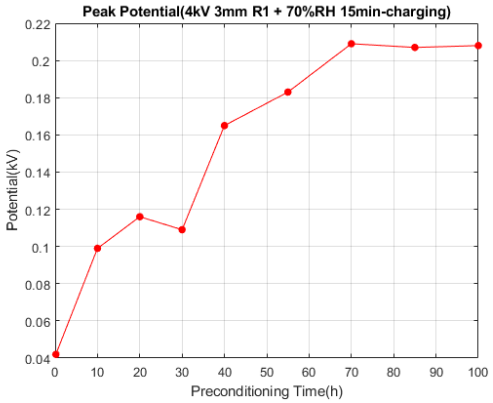

Figure 3.31: Peak Surface Potential After a 15-Minute Charging Following Various Preconditioning Times

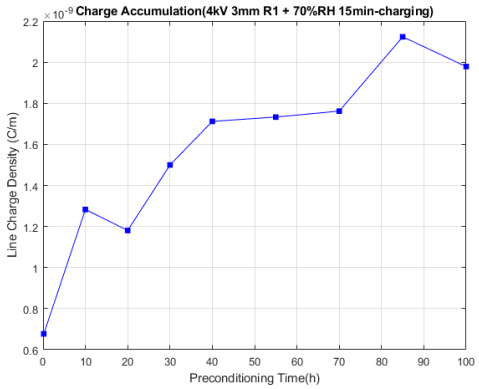

Figure 3.32: Surface Charge Density After a 15-Minute Charging Following Various Preconditioning Times

Observations indicate that the charging rate is minimal during the initial 15-minute period post-treatment, but it increases with longer exposure to humid air until a saturation point is reached. This suggests that preconditioning the electrode is critical

before charging. Two approaches for the preconditioning process are recommended: maintaining a consistent duration for each trial or extending the preconditioning until saturation is achieved.
Based on trial results, we propose the following operational guidelines:

- Maintain humidity levels up to 90% RH to provide a sufficient margin below the condensation threshold of 98% on the electrode surface.
- For testing efficiency, adopt the same preconditioning duration across all test groups to ensure consistent surface conditions, especially when adjustments to the electrode are made.

4

Results and discussions

This chapter presents and interprets the experimental results, organized according to the test matrix outlined in Section 3.2. Section 4.1 describes the initial measurements of potential variation on the surface of the Polycarbonate samples. The line charge density, derived from the surface potential distribution, is represented graphically and approximated using exponential functions. Section 4.2 analyses the influence of humidity on the initial charging, where initial charging rates are calculated and correlated with characteristic variables from different test groups. Section 4.3 compares the findings with those reported in D. Svensson's study [1], highlighting both similarities and differences. Section 4.4 discusses how the electrode surface conditions influence charging behavior, with insights derived from the effects of the preconditioning procedures implemented during the tests.

4.1 Potential variations and line charge density

As described in the test matrix, the setup of each column is considered a distinct test unit. Within each test unit, the charging process is performed at three different humidity levels (RH: 40%, 70%, and 90%). Testing begins at the highest humidity level of 90% RH, following a 10-hour preconditioning of the electrode surface at 90%RH. Subsequent tests are carried out at 70% RH and 40% RH in sequence, without any additional preconditioning. The total charging time for each operation is one hour, with surface potential measurements on the Polycarbonate sample taken at 15-minute intervals, resulting in a total of four readings. This early stage of charging behavior is analyzed using exponential fitting functions to illustrate the overall trend, and their first-order derivatives are employed to assess the charging rate. The various groups in the study are:

- **Voltage variation group:**
  The objective of this test group is to investigate the correlation between charge generation and electric field stress by examining how humidity influences the dynamics of surface charge accumulation on Polycarbonate samples under varying electrode voltages.
  As shown from Figure A.1 to A.3 , at 1 kV, potential changes were recorded below 50V, and the characteristic charging behavior (a Peak-wave pattern) was not observed in the vicinity of the electrode tip. This may be attributed to the potential variations being below the resolution limit of the experimental setup. Alternatively, it is hypothesized that there exists a specific threshold that initiates the charging process. Illustrated from Figure A.4 to A.9, at 2

kV and 4 kV, there was a significant increase over time in the surface potential variations near the electrode tip. The peak potential values, indicative of charging activity, were more pronounced at higher humidity levels and under increased voltage.

Line charge densities, as depicted in Figure 4.1 and 4.2, show a rapid increase within the initial 15 minutes of charging, followed by increases of lower rates, corroborating the findings in D.Svensson's study [1]. Both higher voltages and humidity levels contribute to elevated line charge densities, and more intense charging activity, in accordance with the peak potential observations.

To discern the humidity's varying effects at different voltages, exponential fits were applied to the curves. Table 4.1 indicates that values of $(a \cdot b)$ augment with humidity at both 2 kV and 4 kV, with more pronounced variability at 2 kV. This suggests that humidity may exert a more substantial influence on the charge accumulation dynamics at lower voltages. Given that all controlled variables except voltage remained consistent across different configurations, this implies a stronger influence of humidity on charge generation under lower electrical fields.

Table 4.1: Curve fit of line charge density dynamic for different humidity level in voltage variation group

V (kV)	RH (%)	a	b	$a \cdot b$	Variation Rate: $\frac{a \cdot b(x\%)}{a \cdot b(90\%)}$
1	40	N/A	N/A	N/A	N/A
	70	N/A	N/A	N/A	N/A
	90	N/A	N/A	N/A	N/A
2	40	$2.89 \cdot 10^{-10}$	$2.16 \cdot 10^{-2}$	$6.24 \cdot 10^{-12}$	$1.49 \cdot 10^{-2}$
	70	$4.11 \cdot 10^{-9}$	$4.77 \cdot 10^{-2}$	$19.60 \cdot 10^{-11}$	0.45
	90	$4.62 \cdot 10^{-9}$	$9.05 \cdot 10^{-2}$	$41.81 \cdot 10^{-11}$	1.00
4	40	$7.77 \cdot 10^{-9}$	$6.77 \cdot 10^{-2}$	$52.60 \cdot 10^{-11}$	0.43
	70	$1.89 \cdot 10^{-8}$	$3.86 \cdot 10^{-2}$	$7.30 \cdot 10^{-10}$	0.60
	90	$3.22 \cdot 10^{-8}$	$3.85 \cdot 10^{-2}$	$12.30 \cdot 10^{-10}$	1.00

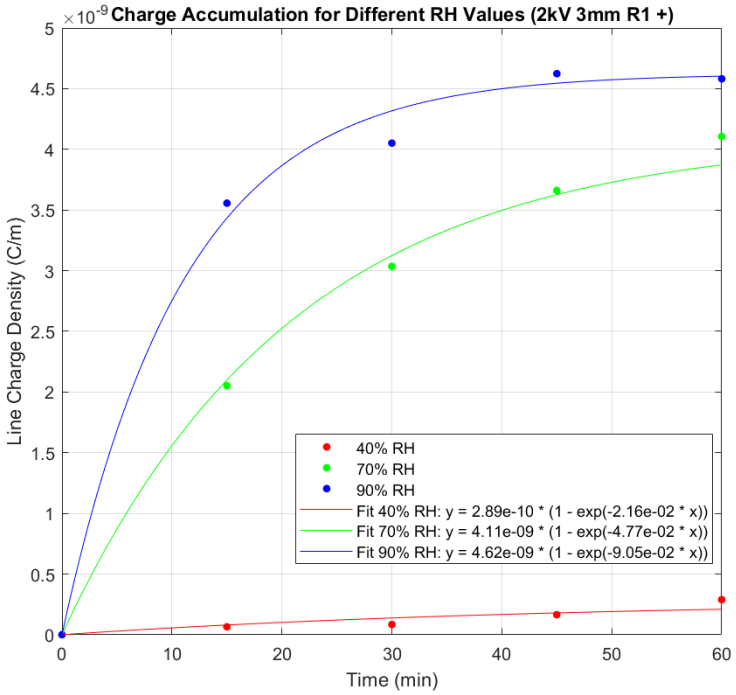

Figure 4.1: Line charge density over time in voltage variation group(V2=2kV,L2=3mm, R1=4mm,Positive Polarity)

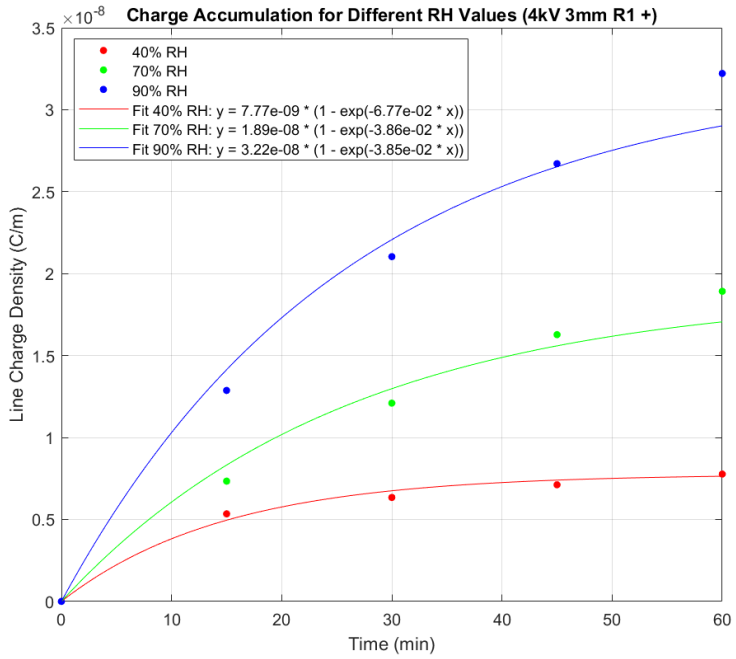

Figure 4.2: Line charge density over time in voltage variation group(V3=4kV,L2=3mm, R1=4mm,Positive Polarity)

- **Air gap length variation group:**
  This test group is designed to study the correlation between charge generation and air volume by investigating the effect of humidity on the dynamics of surface charge accumulation on the Polycarbonate sample across air gaps of varying lengths, which introduce different air volumes.
  Figure A.10 to A.18 show significant potential variations across all cases. When comparing across different humidity levels with the same air gap length, the peak potential consistently rises with humidity, a trend similar to that observed in the voltage group. However, comparing variations in air gap length while maintaining the same humidity reveals no clear relationship. For instance, at 40% RH, the peak potentials ($\sim 0.35\,\mathrm{kV}$) after one hour of charging are comparable for 2mm and 3mm gaps, but much lower ($\sim 0.035\,\mathrm{kV}$) for the 4mm gap. The most significant potential variation at 70% RH occurs with a 3mm gap. While at 90% RH, the greatest variation is seen with a 4mm gap.
  In Table 4.2, values of $(a \cdot b)$ in the time-dependent line charge density curves indicates the highest rate of change occurs with a 4mm gap, followed by a 2mm gap, and the least with a 3mm gap. Hence, the rate of change does not show a direct correlation with the lengths of the air gaps.
  The current findings from the Length group do not establish a definitive relationship between humidity and the dynamics of charge accumulation relative to air gap length. Consequently, a correlation between charge generation and air volume has not been established. It is speculated that other uncontrolled factors may be influencing the charging process. Variations in air gap length alter not only the volume of air but also the distribution of the electric field. Although the initial electric field $E_{\max}$ is normalized by voltage adjustment, field variations throughout the charging process could introduce uncontrolled factors. Furthermore, the electrode surface condition—which influences measurement—is affected by the use of gauge blocks to set air gap lengths. Contact with gauge blocks may alter the electrode surface, and despite consistent preconditioning before charging, initial surface conditions may be inadvertently modified during air gap length calibration.

Table 4.2: Curve fit of line charge density dynamic for different humidity level in air gap length variation group

L(mm)	RH (%)	a	b	$a \cdot b$	Variation Rate: $\frac{a \cdot b(x\%)}{a \cdot b(90\%)}$
2	40	2.50×10^{-9}	1.67×10^{-1}	4.18×10^{-10}	0.36
	70	3.49×10^{-9}	1.11×10^{-1}	3.87×10^{-10}	0.34
	90	1.79×10^{-8}	6.41×10^{-2}	11.47×10^{-10}	1.00
3	40	7.77×10^{-9}	6.77×10^{-2}	52.60×10^{-11}	0.43
	70	1.89×10^{-8}	3.86×10^{-2}	7.30×10^{-10}	0.60
	90	3.22×10^{-8}	3.85×10^{-2}	12.30×10^{-10}	1.00
4	40	8.84×10^{-10}	3.90×10^{-2}	34.48×10^{-12}	2.41×10^{-2}
	70	1.65×10^{-9}	6.46×10^{-2}	10.66×10^{-11}	7.45×10^{-2}
	90	2.58×10^{-8}	5.55×10^{-2}	14.32×10^{-10}	1.00

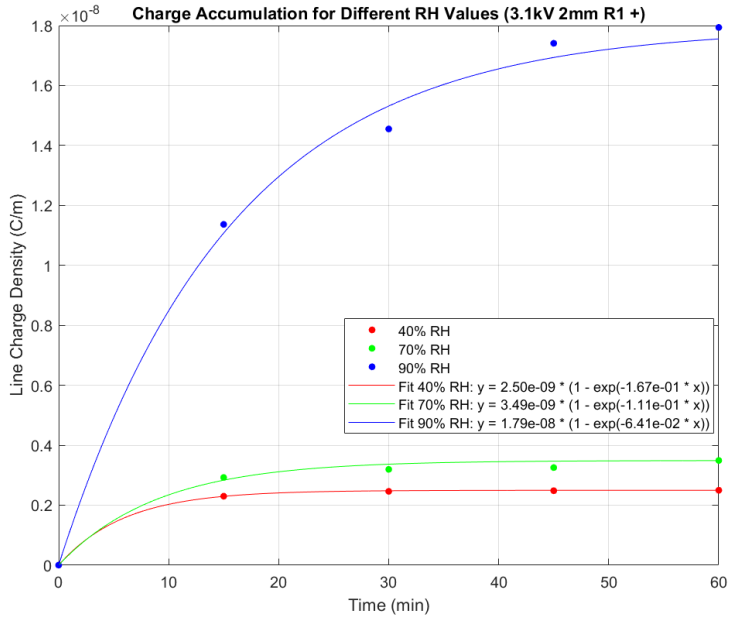

Figure 4.3: Line charge density over time in air gap length variation group(Vx=3.1kV,L1=2mm, R1=4mm,Positive Polarity)

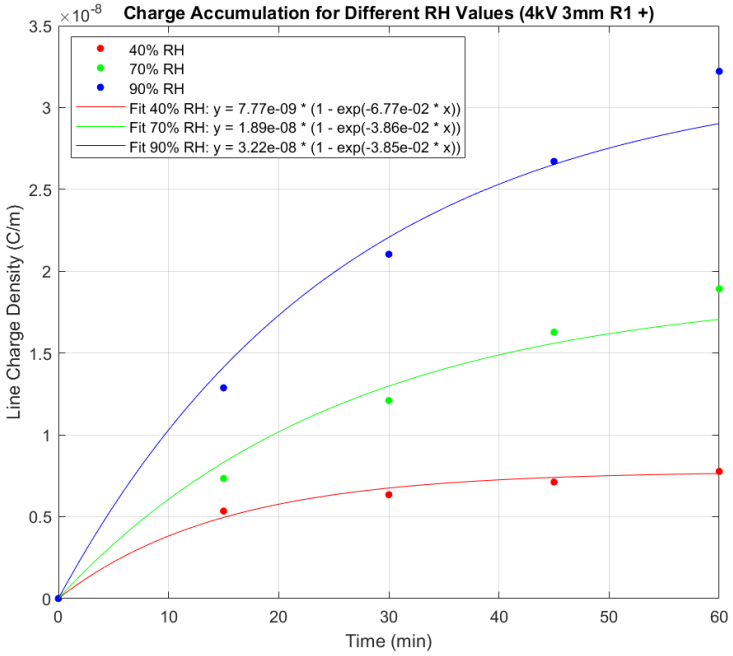

Figure 4.4: Line charge density over time in air gap length variation group(V3=4kV,L2=3mm, R1=4mm,Positive Polarity)

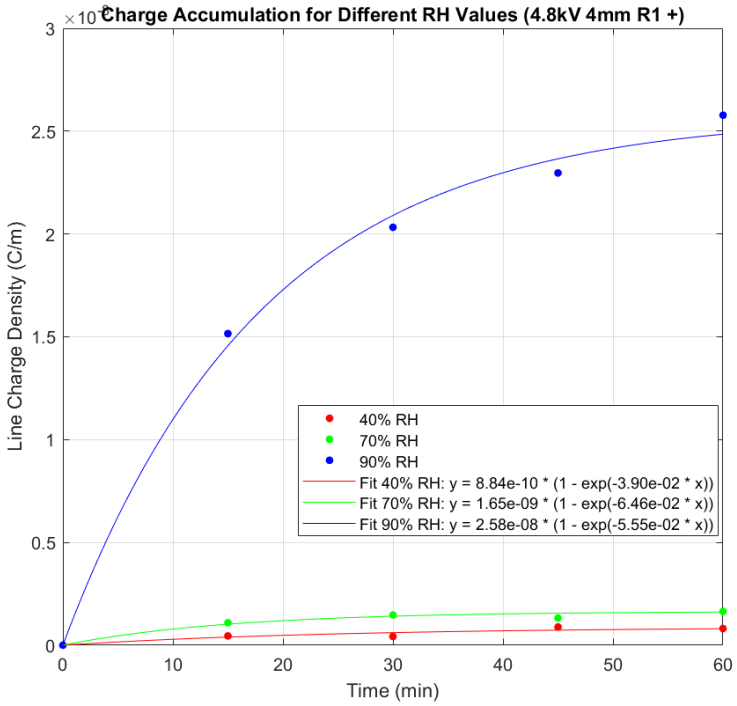

Figure 4.5: Line charge density over time in air gap length variation group(Vy=4.8kV,L3=4mm, R1=4mm,Positive Polarity)

- **Electrode radius variation group:**
  This test group is to study the correlation between charge generation and electrode radius by examining how humidity influences the dynamics of surface charge accumulation on Polycarbonate samples equipped with electrodes of varying radii, which create different charging geometries. Larger electrode radii increase the electrode surface area, air volumes, and homogeneity. This group specifically measures and compares the charging behaviors of electrodes with radii of 4mm and 7mm.
  Figure A.19 to A.24, similar trends are observed where peak potentials at same moments increase with humidity levels, consistent with results from previous groups. However, at 40% humidity with the 7mm radius electrode, charging behavior is undetectable. This may be due to the inherent resolution limits of the experimental setup or potential threshold conditions previously noted in the voltage variation group.
  When comparing electrodes under the same humidity conditions, peak potentials at similar charging times are higher with the 4mm radius electrode than with the 7mm one, suggesting that smaller radii may facilitate a higher charging rate.
  Table 4.3 shows that values of $(a{\cdot}b)$ in the curve functions of line charge density over time exhibit greater variation rate with the larger electrode radius. The results suggest that charging behavior with larger electrode radius is more sensitive to changes in humidity. Therefore, this implies a stronger influence of humidity on charge generation with larger electrode radius.
  However, the repeatability of these results is questionable. The consistency of surface conditions between the two different electrodes cannot currently be verified, which may introduce some measurement uncertainties.

Table 4.3: Curve fit of line charge density dynamic for different humidity level in electrode radius variation group

R(mm)	RH (%)	a	b	$a \cdot b$	Variation Rate: $\frac{a{\cdot}b(x\%)}{a{\cdot}b(90\%)}$
4	40	7.77×10^{-9}	6.77×10^{-2}	52.60×10^{-11}	0.43
	70	1.89×10^{-8}	3.86×10^{-2}	7.30×10^{-10}	0.60
	90	3.22×10^{-8}	3.85×10^{-2}	12.30×10^{-10}	1.00
7	40	N/A	N/A	N/A	N/A
	70	1.33×10^{-10}	5.86×10^{-2}	7.80×10^{-12}	2.36×10^{-2}
	90	5.44×10^{-9}	6.08×10^{-2}	33.08×10^{-11}	1.00

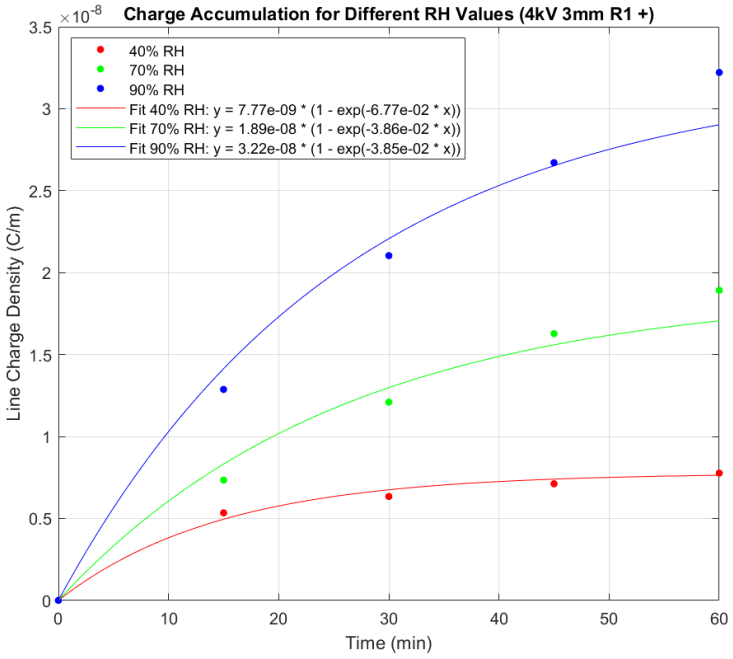

Figure 4.6: Line charge density over time in electrode radius variation group(V3=4kV,L2=3mm, R1=4mm,Positive Polarity)

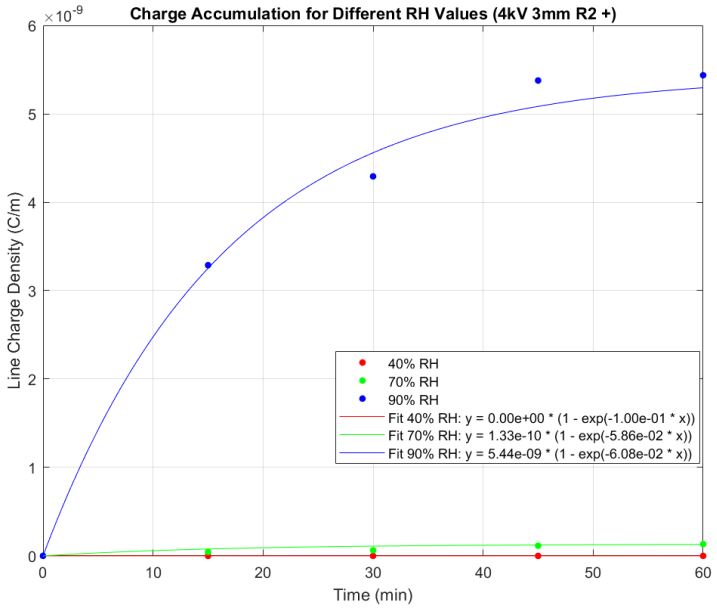

Figure 4.7: Line charge density over time in electrode radius variation group(V3=4kV,L2=3mm, R2=7mm,Positive Polarity)

- **Polarity variation group:**

  This test group aims to study the correlation between charge generation and polarity by exploring how humidity affects the dynamics of charge accumulation on the surface of a Polycarbonate sample under both positive and negative

applied voltages.
As depicted in Figures A.25 and A.30, charging behavior intensifies with higher humidity for both voltage polarities, consistent with findings from other test groups. Notably, at the same humidity levels, peak potential values are higher under positive than negative voltage at the same charging time. This indicates a quicker charging rate under positive polarity, aligning the findings in D.Svensson's study [1]. According to E.Svensson's research [4], one possible explanation involves the electrochemical reactions and ion mobility on the electrode surface, which is speculated to differ with the polarity.
Furthermore, as detailed in Table 4.4, values of $(a \cdot b)$ in the curve functions of line charge density show slightly greater variation under positive polarity. This implies that charging behavior is more responsive to humidity changes under positive polarity, indicating a stronger influence of humidity on charge generation under positive polarity.

Table 4.4: Curve fit of line charge density dynamic for different humidity level in polarity variation group

Polarity	RH (%)	a	b	$a \cdot b$	Variation Rate: $\frac{a \cdot b(x\%)}{a \cdot b(90\%)}$
Positive	40	7.77×10^{-9}	6.77×10^{-2}	52.60×10^{-11}	0.43
	70	1.89×10^{-8}	3.86×10^{-2}	7.30×10^{-10}	0.60
	90	3.22×10^{-8}	3.85×10^{-2}	12.30×10^{-10}	1.00
Negative	40	5.99×10^{-9}	9.01×10^{-2}	53.97×10^{-11}	0.60
	70	1.20×10^{-8}	4.31×10^{-2}	5.17×10^{-10}	0.57
	90	2.16×10^{-8}	4.18×10^{-2}	9.03×10^{-10}	1.00

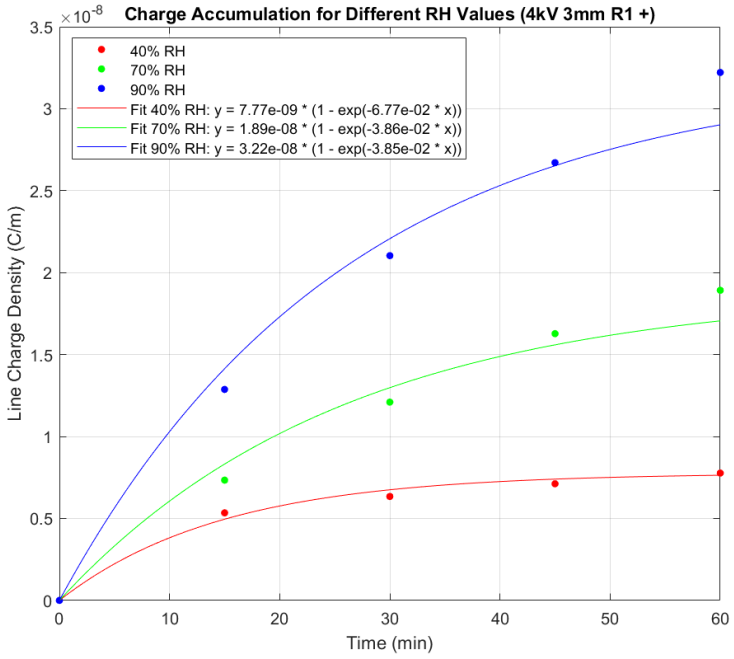

Figure 4.8: Line charge density over time in polarity variation group(V3=4kV,L2=3mm, R1=4mm,Positive Polarity)

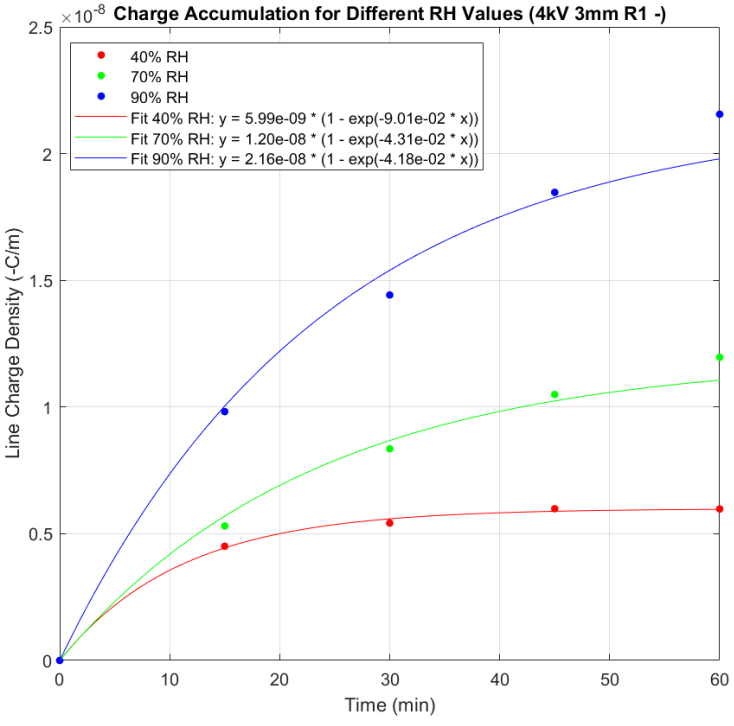

Figure 4.9: Line charge density over time in polarity variation group(V3=4kV,L2=3mm, R1=4mm,Negative Polarity)

4.2 Initial Charging Rate

D.Svensson's study [1] employs the initial charging rate to estimate humidity effects, given the simpler initial electrical field distribution with no charges yet accumulated on the Polycarbonate. This section examines the initial charging rates across various groups to further investigate how humidity influences these rates. The initial charge rates are calculated by employing values of $(a \cdot b)$ from the first-order derivatives of line charge density functions. The maximum electric field strength, $E_{\max}$, which occurs at the electrode tip at the start of charging, is determined using the simulation methods outlined in Section 3.3.

- **Voltage variation group:**
  In this group, all configurations are identical except for the applied voltages, which produce different $E_{\max}$. Relationships between the initial charging rate and $E_{\max}$ across various humidity levels are illustrated in Figure 4.10. Experiments at 1kV, showing no detectable charging, are excluded.
  Comparing initial charging rates at the same humidity level across different $E_{\max}$, there is a higher rate variation at 40% RH compared to 70% RH and 90% RH, indicating a possible higher dependency of the initial charging rate on electrical field strength at lower humidity levels.
  Conversely, comparing rates under the same $E_{\max}$ across different humidity levels, the variation is more consistent at 2.05kV/mm, while a noticeable rate 'jump' between 40% RH and 70% RH is observed at 1.03kV/mm. This suggests a stronger humidity effect on the initial charging rate at lower electrical fields. Alternatively, such 'jumps' in initial charging rate may generally occur between different humidity levels, e.g., below 40% RH at 2.05kV/mm, indicating potential threshold conditions for initial charging behavior.

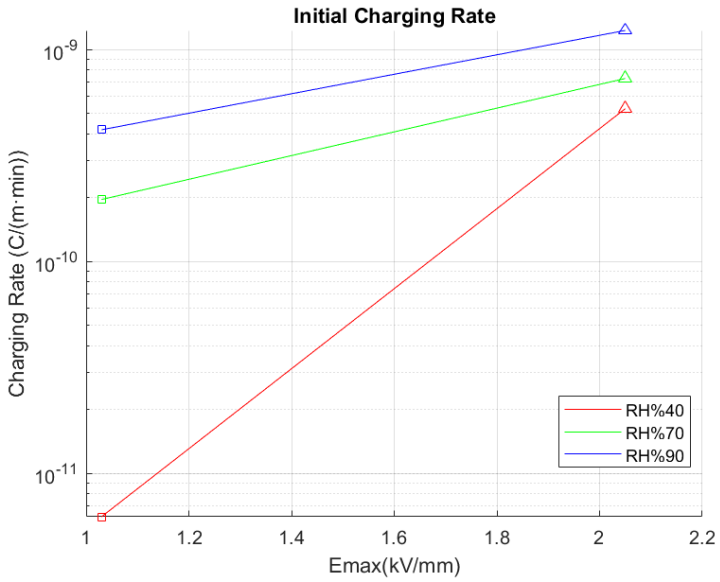

Figure 4.10: Humidity Effect on Initial Charging Rates Under Varied $E_{\max}$ in the Voltage Group

- **Air gap length variation group:**
  Here, varied air gap lengths are employed with a constant $E_{\max}$ of 2.05kV/mm. The initial charging rates at different humidity levels, plotted against varied air gap lengths.
  As depicted in Figure 4.11, there is no consistent increase or decrease in the initial charging rate with increasing air gap lengths. Instead, a slight increase in the initial charging rate is observed at 90% RH, while the fastest rates occur through a 3mm air gap at both 40% RH and 70% RH. Larger rate variations between 70% RH and 90% RH are detected through 2mm and 4mm gaps compared to the 3mm gap.
  The increased uncertainties in the Length group, due to varied air gap lengths creating different homogeneities, are noted. Even with a constant $E_{\max}$, the overall electrical field distribution changes due to these in-homogeneities, including variations on the electrode surface and within the air gap. Moreover, adjustments to air gap lengths may alter electrode surface conditions, complicating the interpretation of humidity effects.

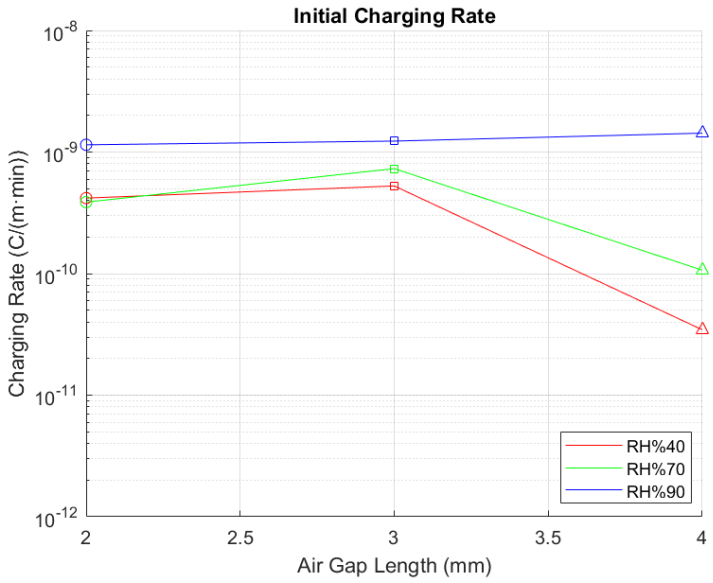

Figure 4.11: Humidity Effect on Initial Charging Rates Under Varied Air Gap Length in the Length Group

- **Electrode radius variation group:**
  Different $E_{\max}$ levels are generated by electrodes of two distinct radii but constant air gap lengths. The initial charging rates across different humidity levels, plotted against varied $E_{\max}$, show larger rate variations at lower humidity levels (70% RH) than at higher humidity levels (90% RH). A rate 'jump' is observed at $E_{\max}$ (1.73 kV/mm), not at higher $E_{\max}$ (2.05 kV/mm).
  These findings align with those in the voltage group, though they are less reliable due to slight volume increases from larger electrode surfaces. The hypothesis regarding initial charging rates and $E_{\max}$, proposed in the voltage group, applies here only if $E_{\max}$ predominantly influences the observed phenomena. Additionally, the consistency of surface conditions between different electrodes remains doubtful.

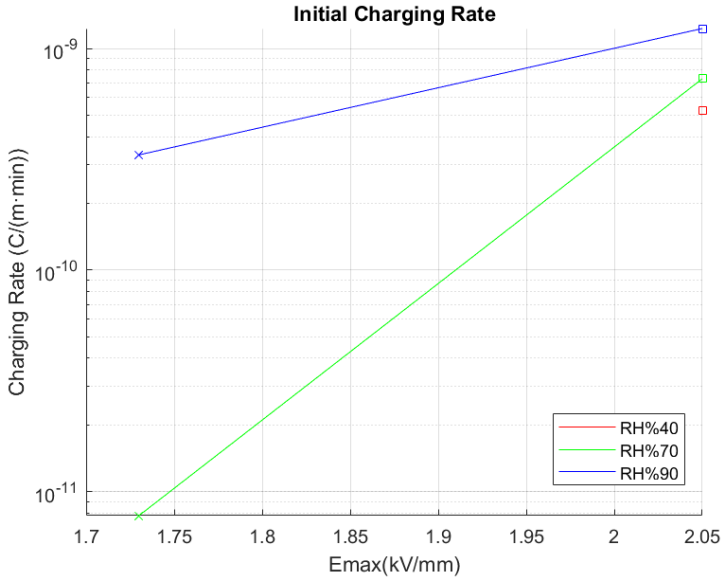

Figure 4.12: Humidity Effect on Initial Charging Rates Under Varied $E_{\max}$ in the Radius Group

- **Polarity variation group:**
  In this test group, the initial conditions, including E_{max} and air gap length, remain constant for both positive and negative polarities. As illustrated in Figure 4.13, the initial charging rate varies more significantly under positive polarity than under negative polarity at the same humidity level. This observation indicates that the impact of humidity on the initial charging rate is polarity-dependent, with positive polarity exhibiting greater sensitivity to humidity changes. The charging rate is more sensitive to humidity under positive polarity. Additionally, the consistency of electrode surface conditions is maintained in this group, as no contact with the electrode is necessary, enhancing the accuracy of the results.

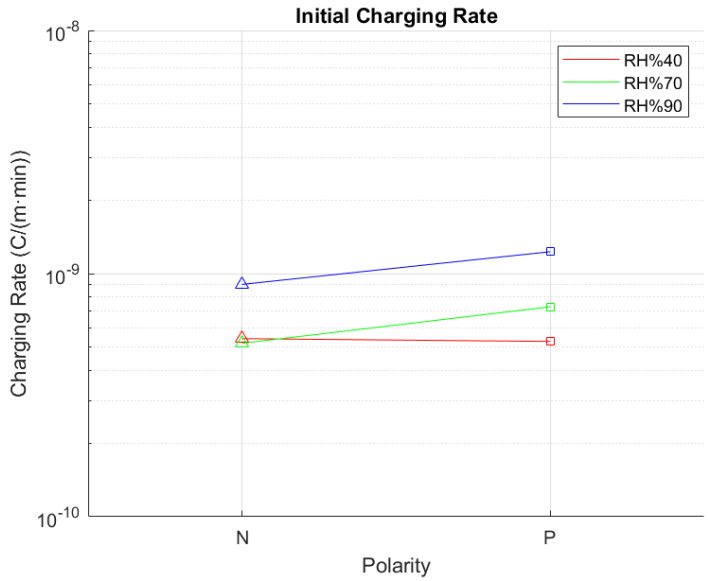

Figure 4.13: Humidity Effect on Initial Charging Rates Under Different Polarities in the Polarity Group

4.3 Comparative analysis with the previous study

Building on D. Svensson's study [1], this research utilizes a similar test chamber structure and identical methods for measuring surface potential to estimate charge accumulation, revealing similar trends in the reference test unit. Both studies observe that peak potential increases with rising humidity levels, as demonstrated from Figure A.7 to A.9, leading to an exponentially saturating line charge density depicted in Figure 4.2. Additionally, Figure A.9 indicates that the distribution of surface potential becomes less symmetric at RH 90%, a pattern also noted in previous studies at humidity levels above RH 90%. Furthermore, similar polarity effects are observed, with a faster charging process under positive polarity, as detailed in Figures 4.8 and 4.9.
However, the introduction of a newly designed humidity control system and an expanded test matrix introduces different experimental procedures and reveals new

phenomena. With a much faster humidity control process, a condensation-like phenomenon is observed on the electrode surface, causing the charging behavior undetectable. This suggests a possible charging-block effect dependent on the electrode surface condition. Similar undetectable charging situations occur at 1kV across all experimental humidity levels and in tests equipped with a larger radius (7mm) electrode at RH 40%. This points to either a possible resolution limit of the experimental setup or threshold conditions corresponding to the interaction between electrical field strength and air humidity.

4.4 Preconditioning of the electrode surface

In the preconditioning test, Figure 3.31 shows that the peak surface potential of each 15-minute charging session increases with longer preconditioning durations and stabilizes after 70 hours. Given the negligible peak surface potential at the initial preconditioning period, it is speculated that the electrode surface condition can be 'reset' by surface treatments, such as cleaning with isopropanol. Subsequently, a time-dependent mechanism is hypothesized to contribute to a stable electrode surface condition. This phenomenon suggests that factors other than electric field strength and air humidity may influence the charging behavior through the electrode surface. Combining the preconditioning test results with the undetectable charging behavior observed when a condensation-like phenomenon occurs on the electrode surface, there appears to be an additional influencing factor on the electrode surface condition, impacting the charge generation mechanism.

5
Conclusion

This study completed the basic tasks outlined in the thesis plan and further enhanced both the experimental setup and theoretical modeling. A simulation model of the charge accumulation dynamics was developed, based on the Maxwell-Wagner capacitor model and the air conductivity's dependence on electrical field strength and humidity. Furthermore, an improved experimental setup equipped with a separate humidity control system was installed. This new setup allows for adjustable test configurations, including voltage, air gap length, electrode radius, and polarity. A test matrix was designed to organize the experiments and categorize the tests. Measurements of charge accumulation dynamics were performed on a Polycarbonate sample under various configurations.

Within the experimental humidity range of 40% to 90%, results indicate that the effect of humidity on charge accumulation dynamics at the dielectric-air interface varies across different test conditions such as voltage levels, air gap lengths, electrode radii, and polarities. The interface charging behavior exhibits higher sensitivity to air humidity at lower voltage levels and under positive polarities, demonstrated by a higher rate of line charge density variation with increasing humidity levels. A similar trend occurs with larger electrode radii, though these results are less repeatable due to uncertain electrode surface conditions. The sensitivity of interface charging behavior to air humidity across different air gap lengths remains unclear due to complex measurement results. Based on the analysis of initial charging rates, it is hypothesized that initial charging behavior is more responsive to air humidity at lower electrical field strengths and positive polarity. The influence of air volume on initial charging conditions has not been definitively established.

The newly implemented humidity control system has not only significantly improved the control over testing conditions but also underscored the potential role of electrode surface conditions in influencing charge generation. Referring to the observed phenomenon where no charging behaviors observed with water condensation on electrode surfaces, it is hypothesized that charge generation primarily takes place on the electrode surface, and a thick water film may mask the emission of free charges. Experimental results from studies on charge accumulation dynamics indicate that charge generation depends on the interaction between air humidity and electric field stress, with polarity playing a significant role. Additionally, preconditioning tests suggest that time-dependent dynamics on the electrode surface may also impact the charge generation mechanism. However, the effect of air volume on this mechanism remains uncertain.

6
Future Work

This chapter outlines suggested areas for future research based on the findings and limitations encountered in this thesis. Throughout this study, various measurements were conducted under different configurations, leading to several hypotheses. However, due to the limitations in measurement accuracy and data sufficiency, no definitive conclusions could be drawn regarding the mechanisms of charge generation in humid air below the electron avalanche onset voltage. This section discusses potential improvements and further investigations that could enhance the understanding and reliability of future studies.

- **Experimental Setup**
  The upgraded experimental setup, equipped with a rapid-response humidity control system and flexible electrode adjustment, allowed for varied humidity levels and testing configurations. Despite these improvements, the manual adjustment of electrodes and air gap lengths could introduce uncontrolled variables and potential measurement errors. To mitigate this, it is recommended to develop a mechanical structure with an automated air gap length calibration system that allows for adjustments without direct contact. This would minimize possible disturbances to the electrode surface conditions and enhance measurement reliability.
- **Experimental Procedure**
  To address the challenge of covering various experimental configurations within a limited thesis period, the repeatability of the test results has not been sufficiently verified, leading to measurement uncertainties. To enhance experimental reliability, it is recommended to conduct additional repeat tests for more statistically robust results. Further investigations into measurement uncertainties are also advised. Moreover, increasing the frequency of measurements during the first 15 minutes of charging could improve the resolution of initial charging data, given the rapid changes in charging rate at this early stage.
- **Electrode Surface Condition**
  The impact of water layer thickness on the electrode surface and its influence on charging behavior are crucial and unclear. It should be clarified whether threshold or masking conditions exist. Moreover, although a preconditioning process has been used to standardize electrode surface conditions, the consistency of this approach is difficult to assess. Future work should focus on developing methods to measure electrode surface conditions accurately and conduct preconditioning tests across electrodes of different materials and humidity levels. Additionally, investigating the dynamics of electrode surface conditions during preconditioning could provide deeper insights into the mechanisms of

charge generation.

- **Humidity testing range**
  The humidity range tested in this study was 40% to 90% RH, which does not encompass the full range encountered in outdoor HVDC equipment operations, particularly in dry regions or extremely humid conditions. To validate the hypothesis that lower electrical fields have a stronger humidity effect, it is crucial to extend testing to include humidity levels below 40%. Additionally, comprehensive testing across a broader range of humidity levels would enhance the robustness and applicability of the data.
- **Modeling**
  The current mathematical model, based on a homogeneous dielectric configuration, does not adequately represent the inhomogeneous setups used in the experiments. A more detailed model that accounts for both homogeneous and inhomogeneous conditions at the dielectric-air interface would likely provide more accurate simulations of the charge accumulation dynamics. Such a model would be invaluable for predicting experimental outcomes and verifying the operational accuracy of experimental setups. Additionally, more advanced modeling can be pursued, including ion-drift models that incorporate ionic source terms, for further analysis of the test results.
- **Interaction between humidity and electric field stress**
  This study's experimental results suggest that an interaction between humidity and electric field stress may play a role in charge generation mechanisms, requiring further investigation. Exploring possible threshold RH values or electric field stress levels that initiate charge generation is recommended. Identifying such threshold conditions could enhance our understanding of how both factors contribute to charge generation mechanisms

Future investigations based on these recommendations are expected to refine the understanding of charge accumulation dynamics significantly, addressing the existing gaps in knowledge and improving the technological applications related to HVDC systems.

Bibliography

[1] Daniel Svensson. Humidity dependence of charge accumulation on polymer-air interfaces for hvdc applications. 2020.

[2] Tianyu Wang, Xiaofen Li, Boya Zhang, Dayu Li, Jianbo Liu, and Guixin Zhang. Basic reason for the accumulation of charge on the surface of polymer dielectrics. *Science China Materials*, 65(10):2884–2888, 2022.

[3] Poliana Duarte Mundim, Henrik Löfås, Nils Lavesson, and Venkatesulu Bandapalle. Ion current measurements in air for hvdc applications. In *2018 IEEE 2nd International Conference on Dielectrics (ICD)*, pages 1–4. IEEE, 2018.

[4] Erik Svensson. Humidity dependent conductivity of air in hvdc applications and the role of surfaces, 2023.

[5] Daniel Svensson, Sarath Kumara, Olof Hjortstam, and Yuriy V. Serdyuk. Effect of humidity on charge accumulation on polymer-air interfaces under dc stress. In *Proceedings of the IEEE International Conference on Dielectrics (ICD)*, Gothenburg, Sweden, 2022. IEEE, IEEE.

[6] Andreas Küchler. *High Voltage Engineering: Fundamentals-Technology-Applications*. Springer, 2017.

[7] David Keun Cheng et al. *Field and wave electromagnetics*. Pearson Education India, 1989.

[8] Josef Kindersberger and Christoph Lederle. Surface charge decay on insulators in air and sulfurhexafluorid - part i: simulation. *IEEE Transactions on Dielectrics and Electrical Insulation*, 15(4):941–948, 2008.

[9] Sarath Kumara, Yuriy V Serdyuk, and Stanislaw M Gubanski. Surface charge decay on polymeric materials under different neutralization modes in air. *IEEE Transactions on Dielectrics and Electrical Insulation*, 18(5):1779–1788, 2011.

[10] Refrigerating American Society of Heating and Inc. (ASHRAE) Air-Conditioning Engineers. *2021 ASHRAE® Handbook - Fundamentals (I-P Edition)*. American Society of Heating, Refrigerating and Air-Conditioning Engineers, Inc. (ASHRAE), 2021.

[11] M Kochsiek. Measurement of water adsorption layers on metal surfaces. *Metrologia*, 18(3):153, 1982.

[12] Chen Xiao, Pengfei Shi, Wenmeng Yan, Lei Chen, Linmao Qian, and Seong H Kim. Thickness and structure of adsorbed water layer and effects on adhesion and friction at nanoasperity contact. *Colloids and Interfaces*, 3(3):55, 2019.

[13] Eric M Stuve. Ionization of water in interfacial electric fields: An electrochemical view. *Chemical Physics Letters*, 519:1–17, 2012.

[14] Christopher J Rothfuss, Valentin K Medvedev, and Eric M Stuve. Temperature and field dependence of protonated water cluster emission from field adsorbed water layers on platinum. *Surface science*, 501(3):169–181, 2002.

[15] Christopher J Rothfuss, Valentin K Medvedev, and Eric M Stuve. The influence of the surface electric field on water ionization: a two step dissociative ionization and desorption mechanism for water ion cluster emission from a platinum field emitter tip. *Journal of Electroanalytical Chemistry*, 554:133–143, 2003.

[16] H Over and AP Seitsonen. Oxidation of metal surfaces. *Science*, 297(5589):2003–2005, 2002.

[17] Jiang Xingliang, Zhao Shihua, Xie Yanbin, Zhang Zhijin, and Shu Lichun. Study on fog flashover performance and fog-water conductivity correction coefficient for polluted insulators. *IET Generation, Transmission & Distribution*, 7(2):145–153, 2013.

[18] Anthony Reginald Blythe and David Bloor. *Electrical properties of polymers*. Cambridge university press, 2005.

[19] Psg teflon ptfe. `https://catalog.wshampshire.com/Asset/psg_teflon_ptfe.pdf`. Accessed: 2024-04-17.

[20] Elena Seran, Michel Godefroy, E Pili, Nathalie Michielsen, and Sylvain Bondiguel. What we can learn from measurements of air electric conductivity in 222rn-rich atmosphere. *Earth and Space Science*, 4(2):91–106, 2017.

[21] Thi Thu Nga Vu, Gilbert Teyssedre, Séverine Le Roy, and Christian Laurent. Maxwell–wagner effect in multi-layered dielectrics: interfacial charge measurement and modelling. *Technologies*, 5(2):27, 2017.

[22] Lewis Greenspan. Humidity fixed points of binary saturated aqueous solutions. *Journal of research of the National Bureau of Standards. Section A, Physics and chemistry*, 81(1):89, 1977.

[23] Florian Küchler, Elias Ramon Lötscher, Raphael Färber, and CM Franck. Polarization-depolarization current (pdc) measurements for volume and surface resistivity analysis of polymeric materials. In *2021 IEEE Conference on Electrical Insulation and Dielectric Phenomena (CEIDP)*, pages 17–22. IEEE, 2021.

A

Appendix 1

This appendix presents the original measurements of potential variations over time on the Polycarbonate surface in different test groups.

A.1 Voltage Group

Configuration: V1=1kV, L2=3mm, R1=4mm, Positive Polarity

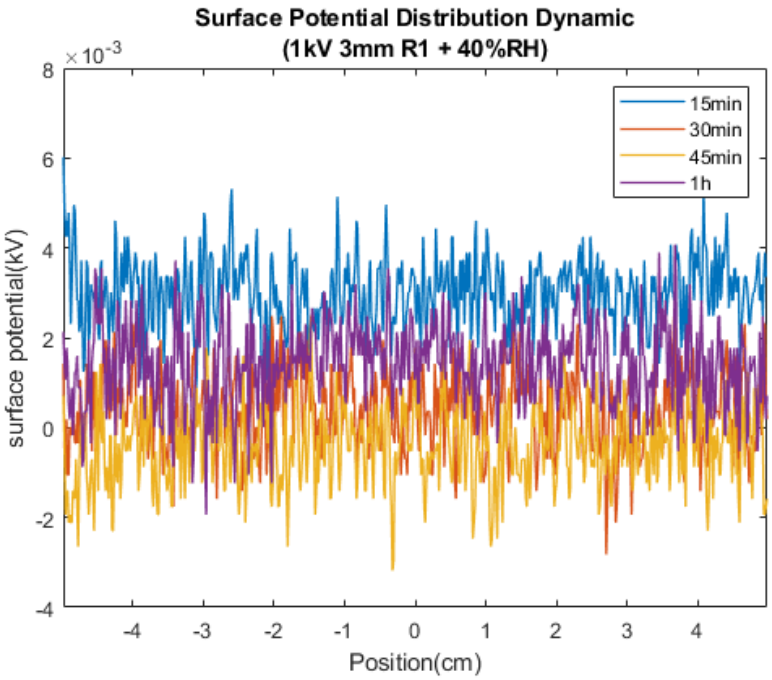

Figure A.1: Potential Variations at 40% RH in Voltage Group (V1=1kV)

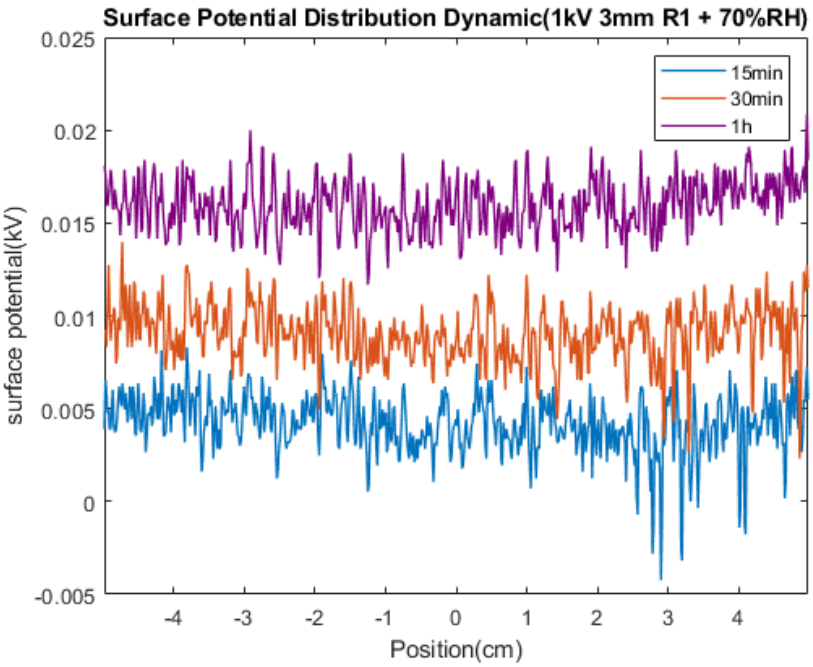

Figure A.2: Potential Variations at 70% RH in Voltage Group (V1=1kV)

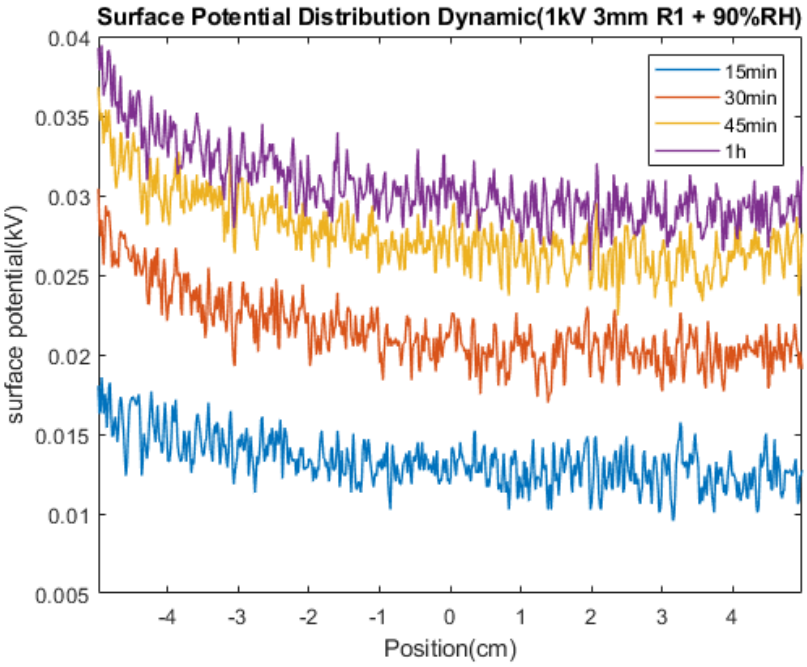

Figure A.3: Potential Variations at 90% RH in Voltage Group (V1=1kV)

Configuration: V2=2kV, L2=3mm, R1=4mm, Positive Polarity

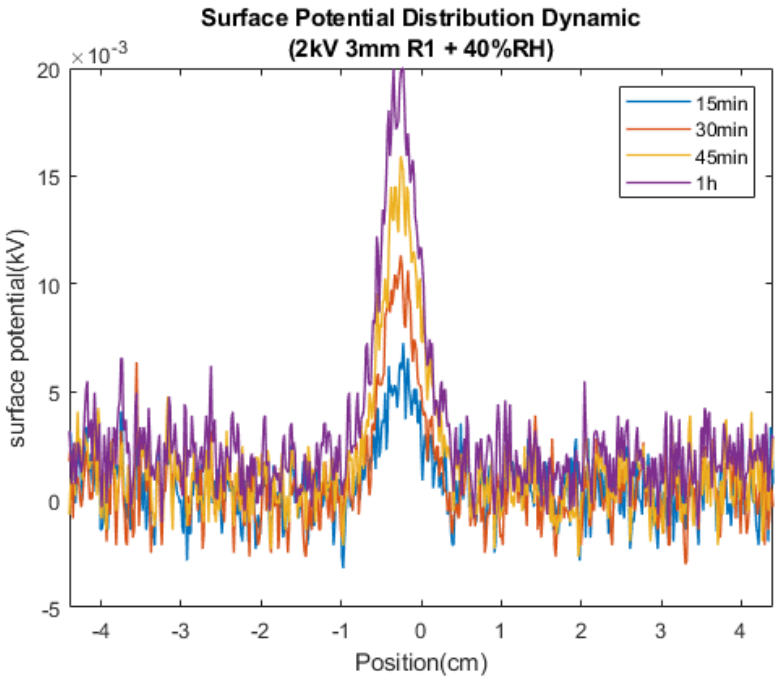

Figure A.4: Potential Variations at 40% RH in Voltage Group (V2=2kV)

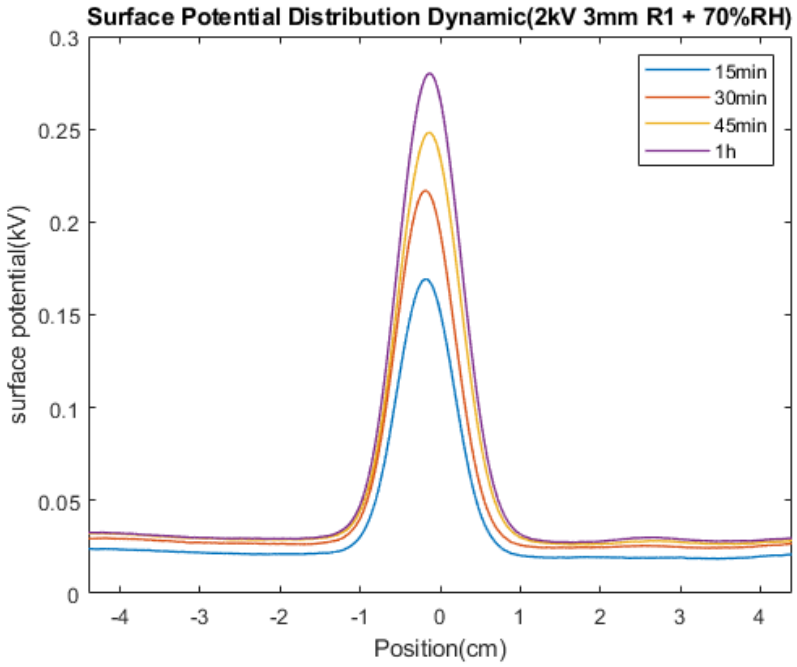

Figure A.5: Potential Variations at 70% RH in Voltage Group (V2=2kV)

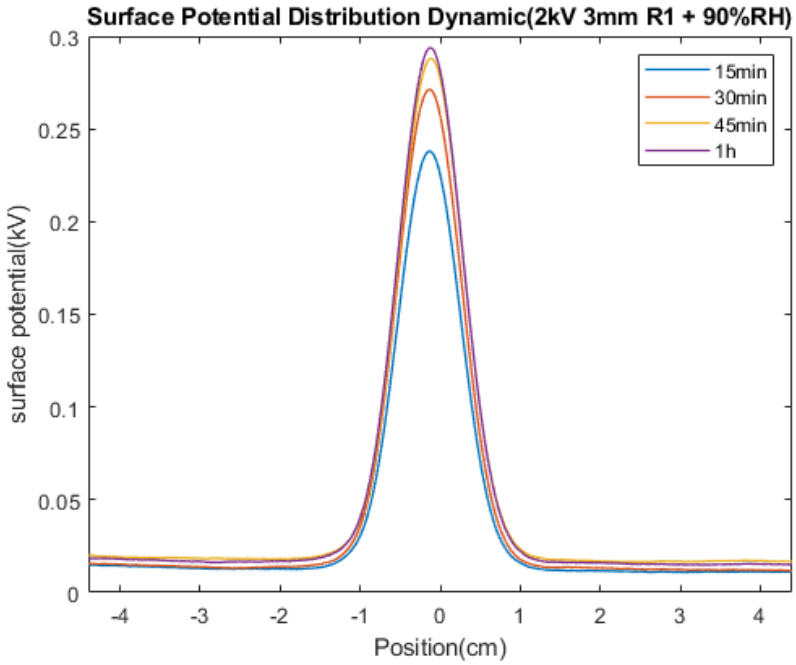

Figure A.6: Potential Variations at 90% RH in Voltage Group (V2=2kV)

Configuration: V3=4kV, L2=3mm, R1=4mm, Positive Polarity

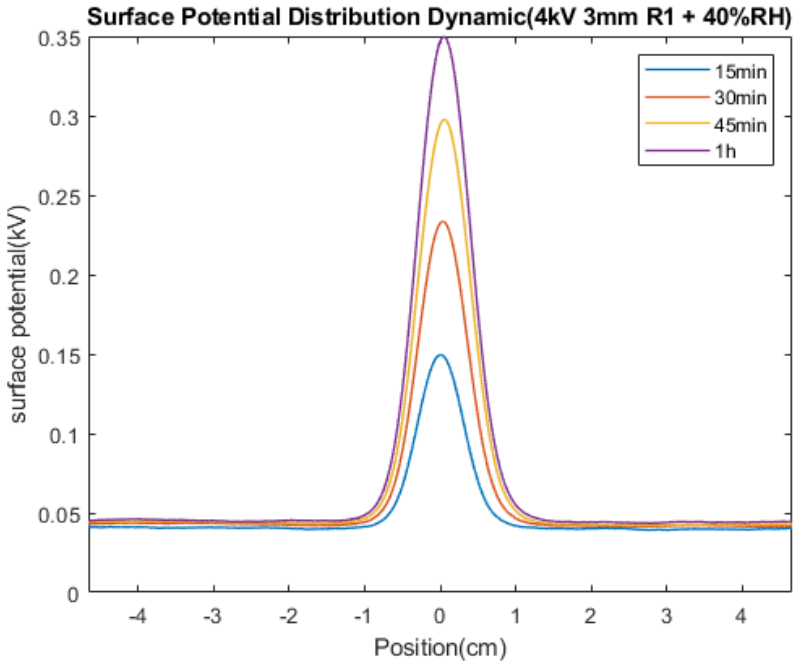

Figure A.7: Potential Variations at 40% RH in Voltage Group (V3=4kV)

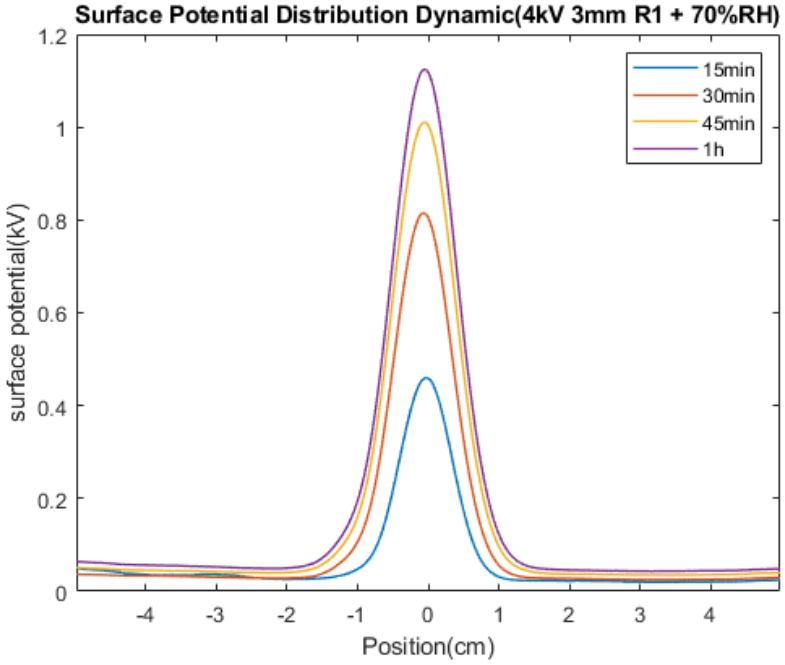

Figure A.8: Potential Variations at 70% RH in Voltage Group (V3=4kV)

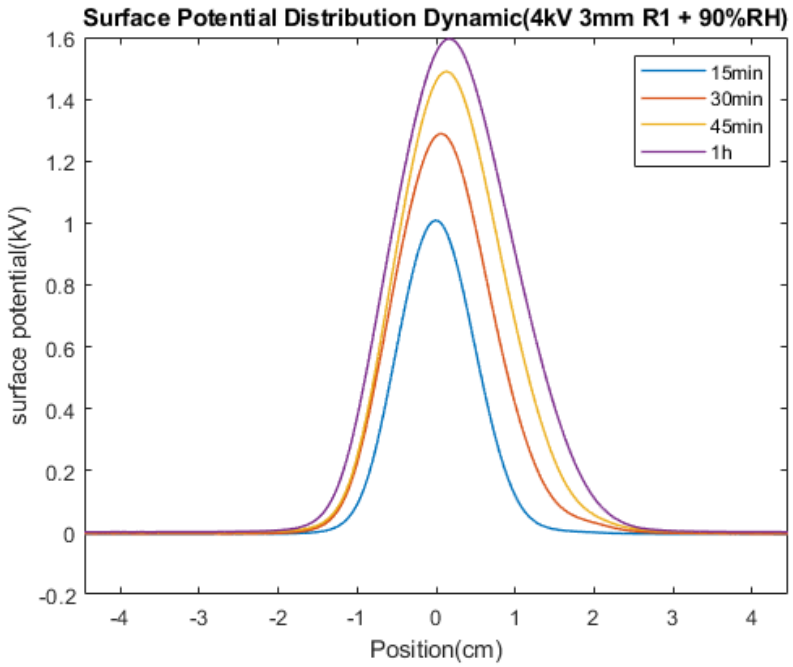

Figure A.9: Potential Variations at 90% RH in Voltage Group (V3=4kV)

A.2 Length Group

Configuration: Vx=3.1kV, L1=2mm, R1=4mm, Positive Polarity

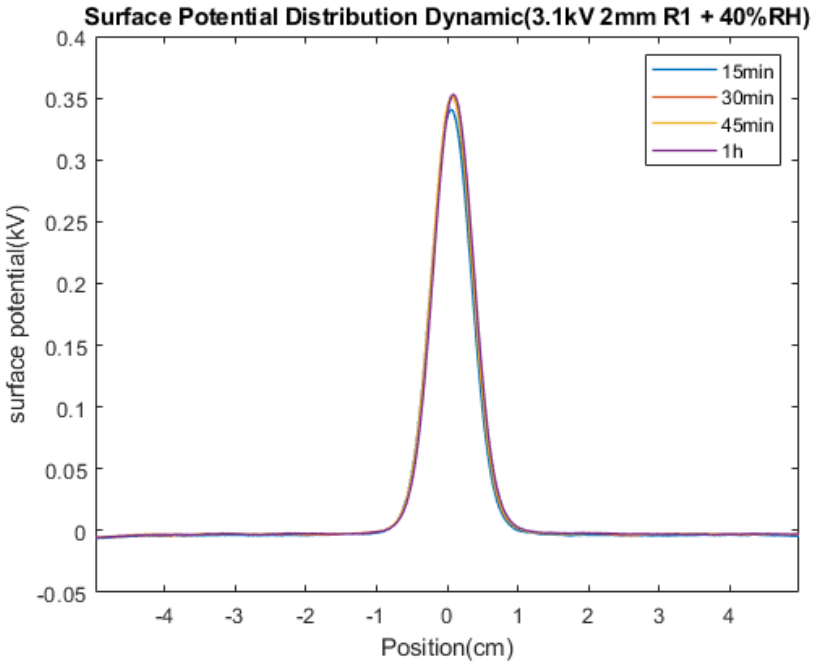

Figure A.10: Potential Variations at 40% RH in Length Group (Vx=3.1kV, L1=2mm)

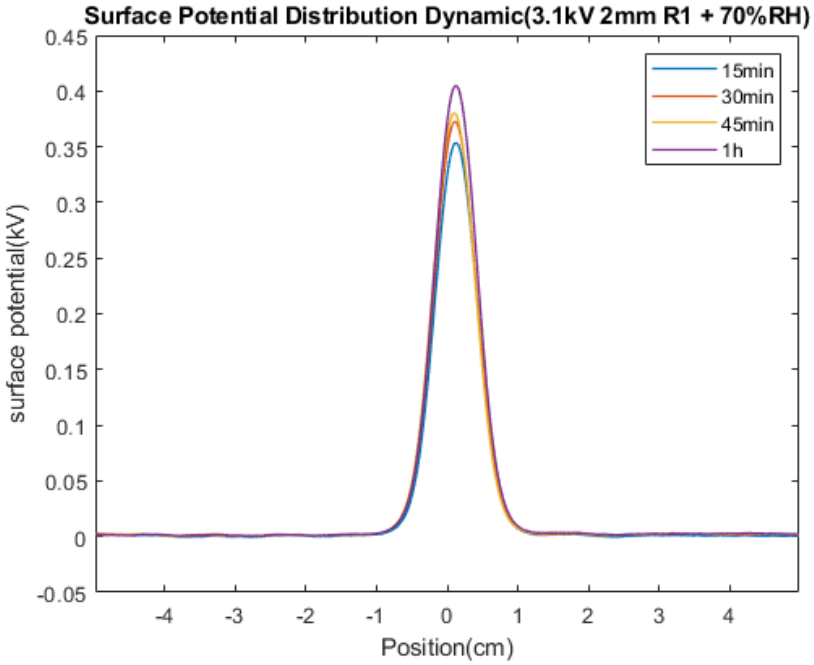

Figure A.11: Potential Variations at 70% RH in Length Group (VX=3.1kV, L1=2mm)

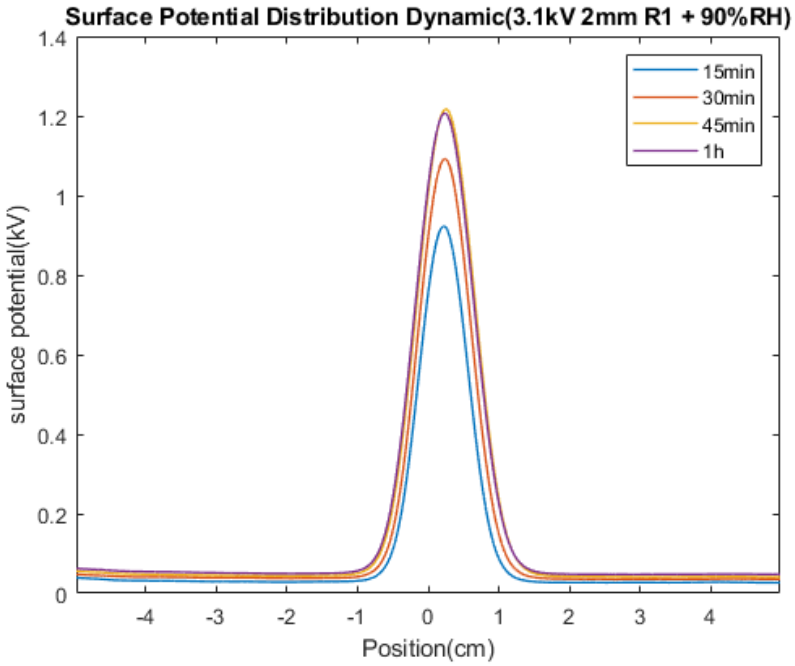

Figure A.12: Potential Variations at 90% RH in Length Group (VX=3.1kV, L1=2mm)

Configuration: V3=4kV, L2=3mm, R1=4mm, Positive Polarity

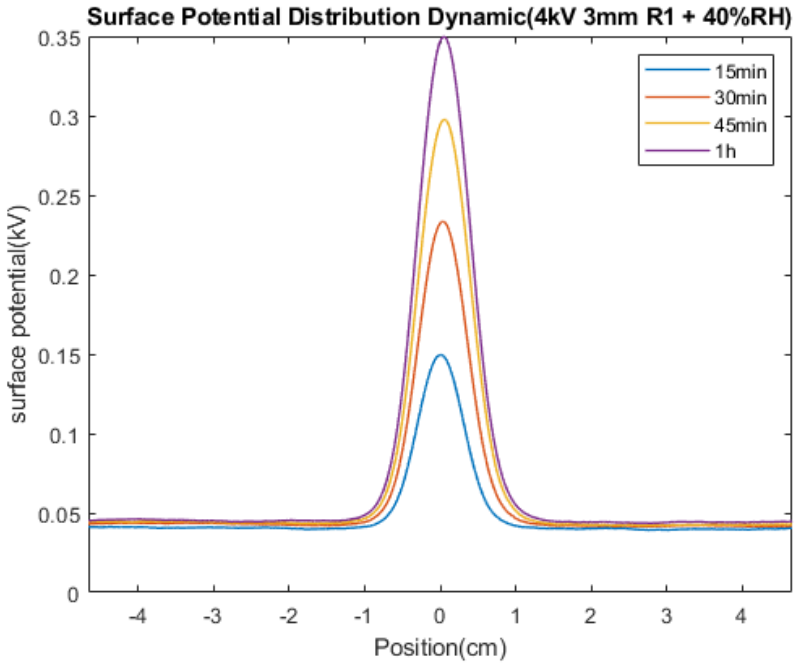

Figure A.13: Potential Variations at 40% RH in Length Group (V3=4kV, L2=3mm)

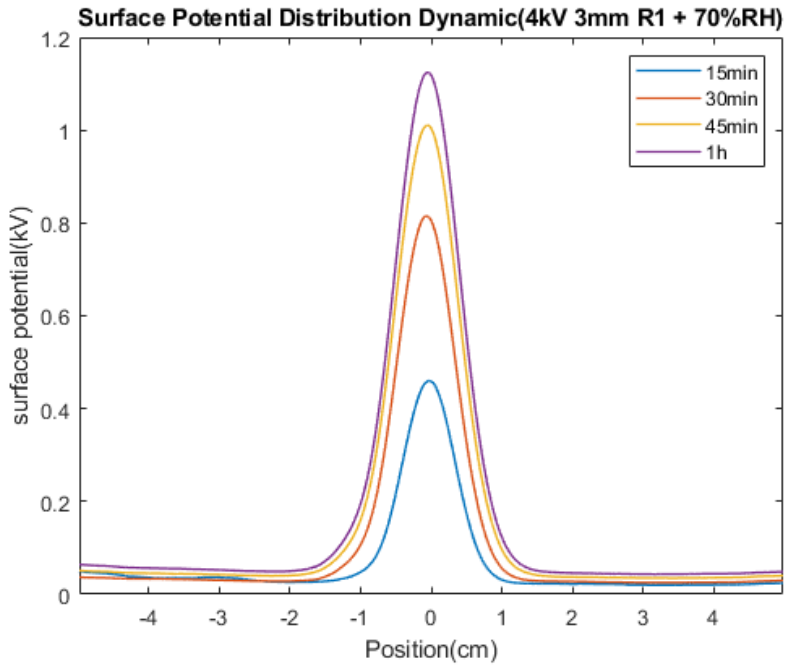

Figure A.14: Potential Variations at 70% RH in Length Group (V3=4kV, L2=3mm)

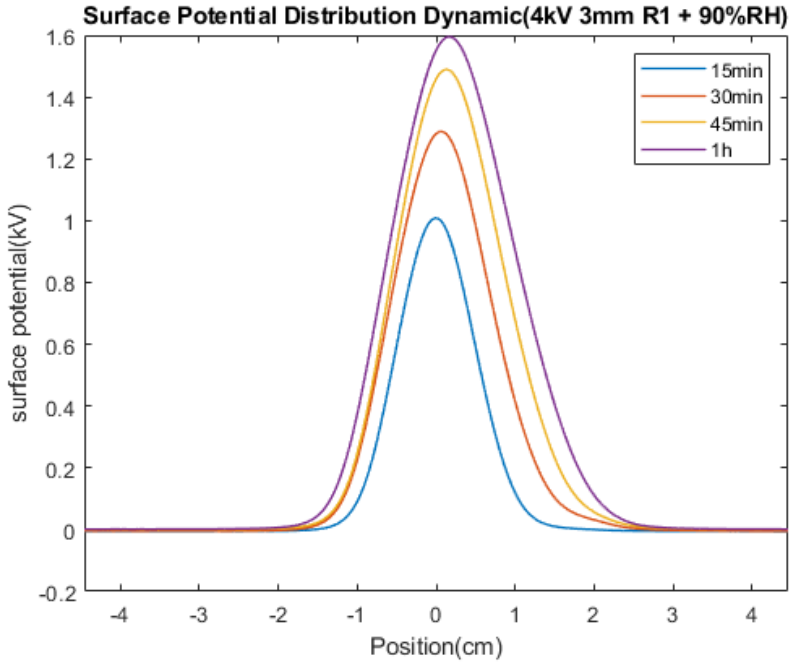

Figure A.15: Potential Variations at 90% RH in Length Group (V3=4kV, L2=3mm)

Configuration: Vy=4.8kV, L3=4mm, R1=4mm, Positive Polarity

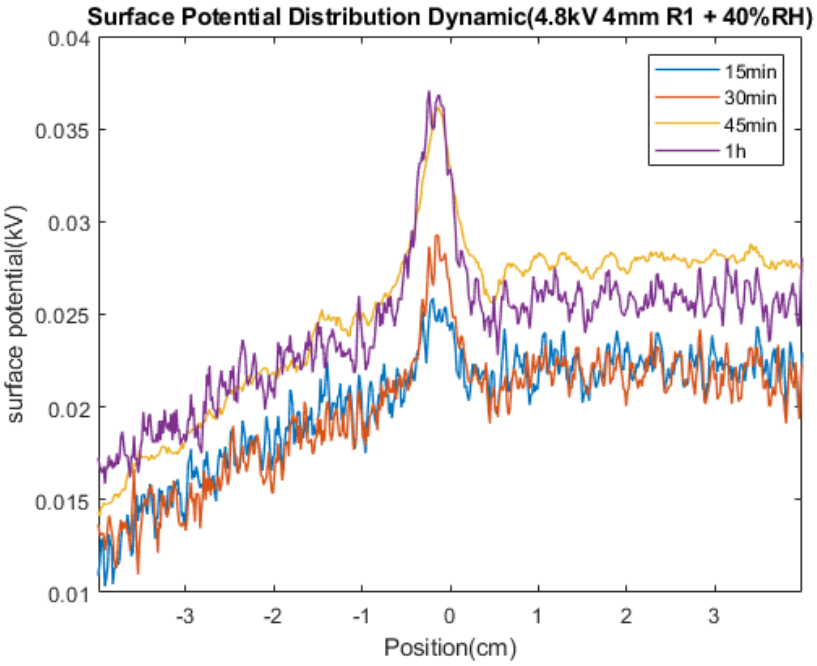

Figure A.16: Potential Variations at 40% RH in Length Group (Vy=4.8kV, L3=4mm)

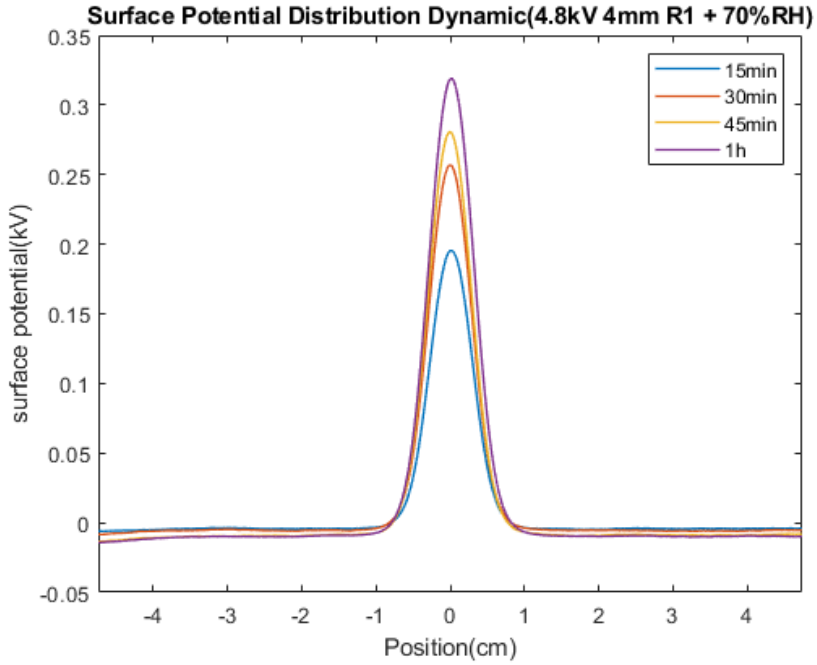

Figure A.17: Potential Variations at 70% RH in Length Group (Vy=4.8kV, L3=4mm)

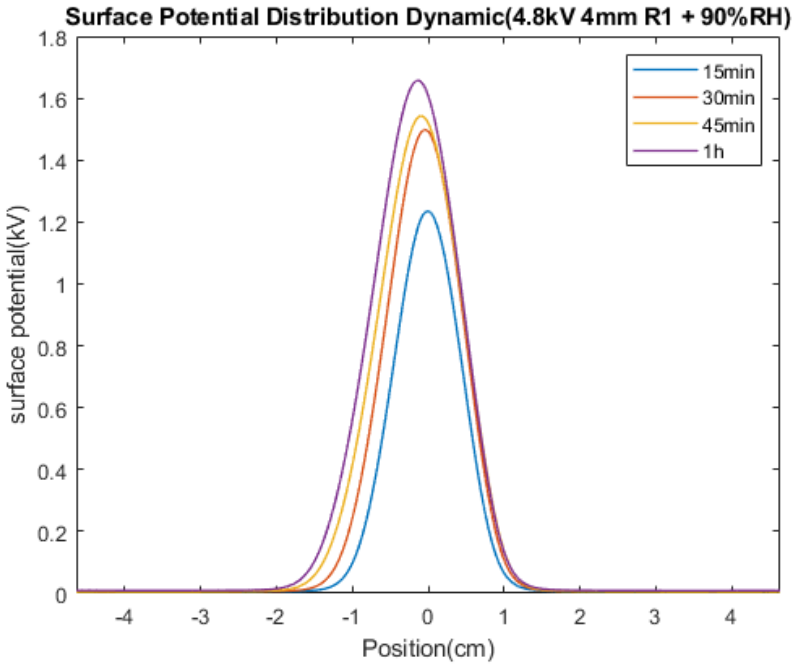

Figure A.18: Potential Variations at 90% RH in Length Group (Vy=4.8kV, L3=4mm)

A.3 Radius Group

Configuration: V3=4kV, L2=3mm, R1=4mm, Positive Polarity

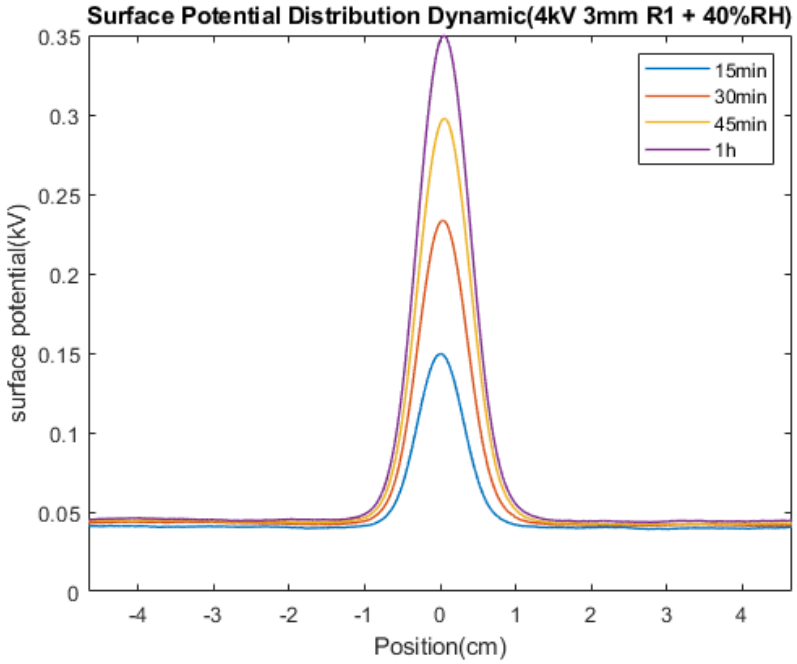

Figure A.19: Potential Variations at 40% RH in Radius Group (R1=4mm)

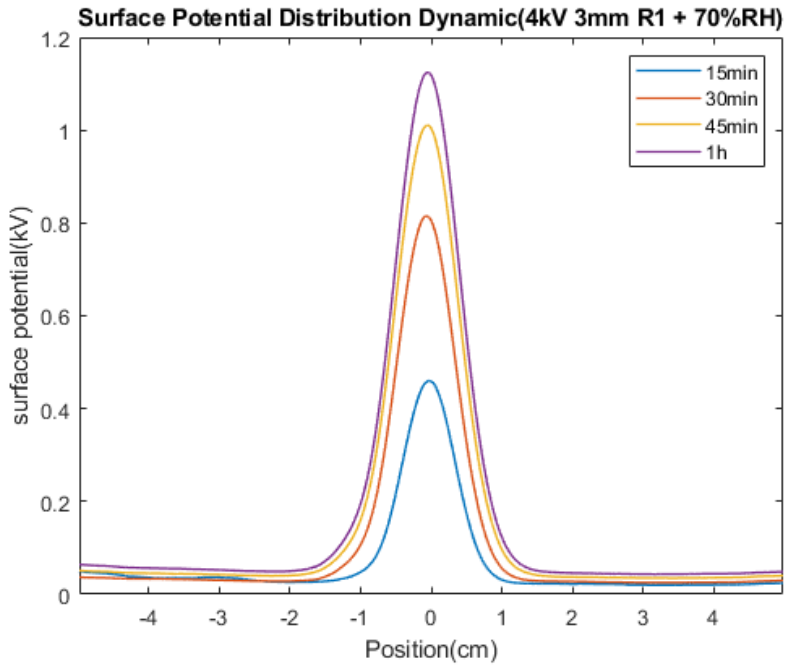

Figure A.20: Potential Variations at 70% RH in Radius Group (R1=4mm)

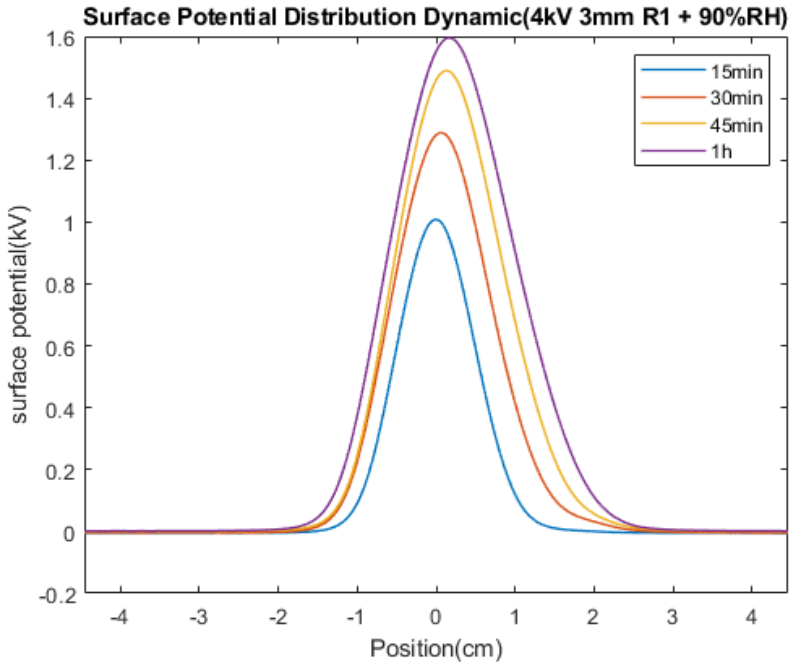

Figure A.21: Potential Variations at 90% RH in Radius Group (R1=4mm)

Configuration: V3=4kV, L2=3mm, R2=7mm, Positive Polarity

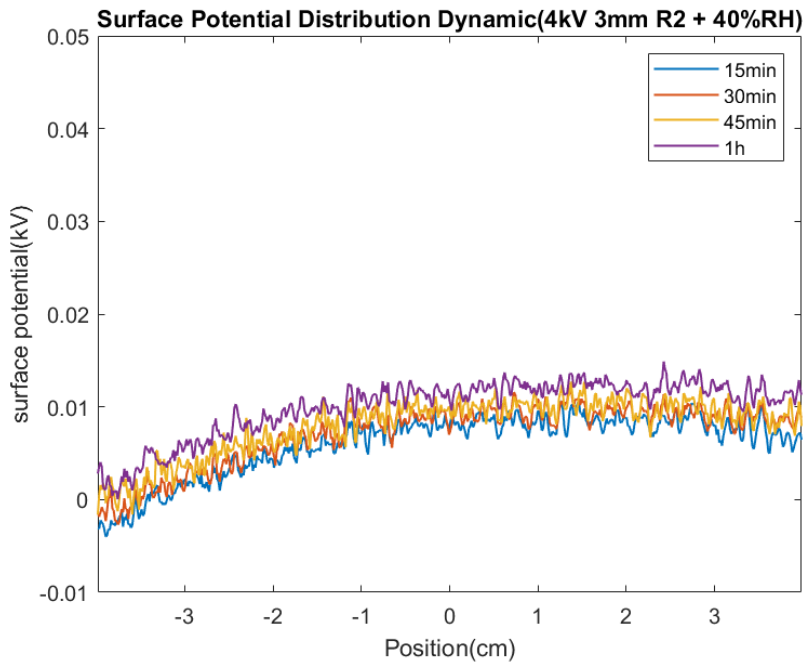

Figure A.22: Potential Variations at 40% RH in Radius Group (R1=4mm)

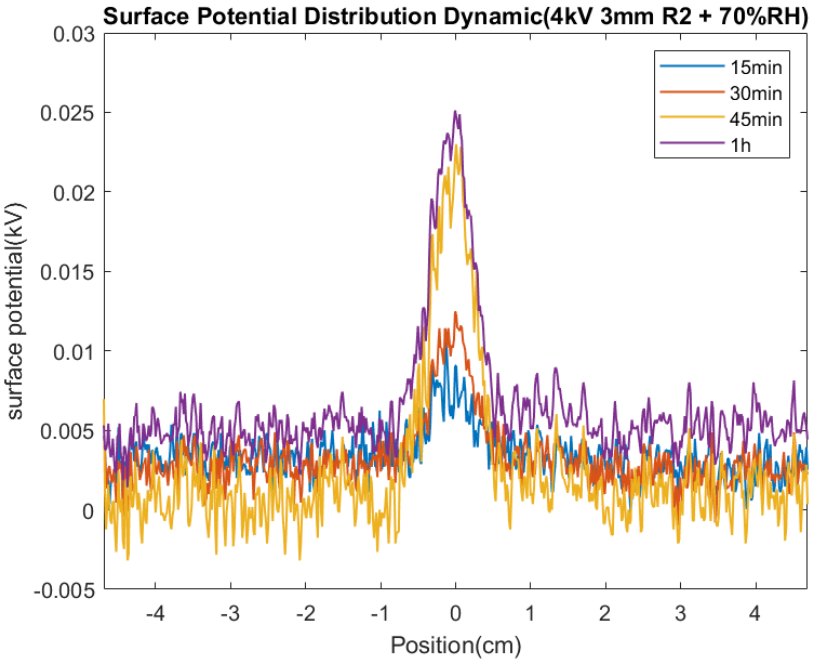

Figure A.23: Potential Variations at 70% RH in Radius Group (R1=4mm)

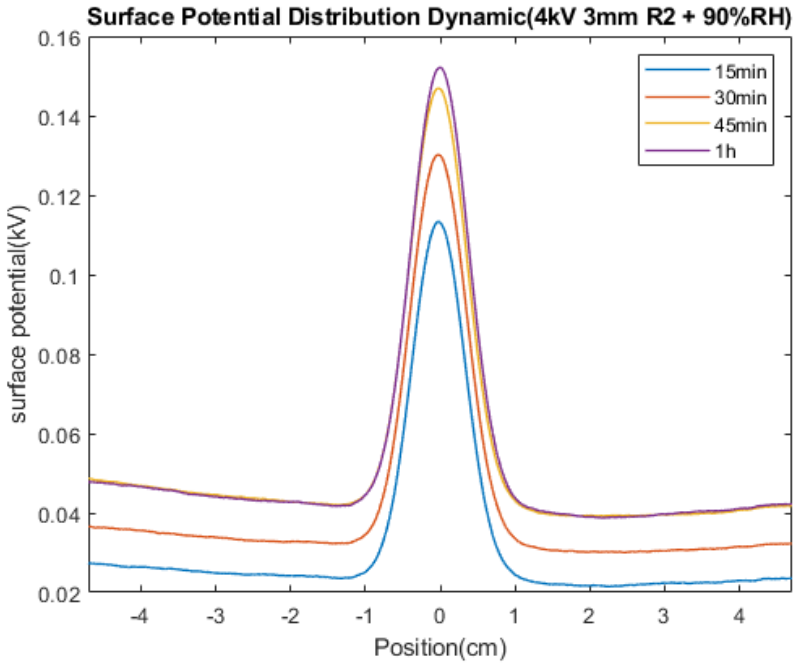

Figure A.24: Potential Variations at 90% RH in Radius Group (R1=4mm)

A.4 Polarity Group

Configuration: V3=4kV, L2=3mm, R1=4mm, Positive Polarity

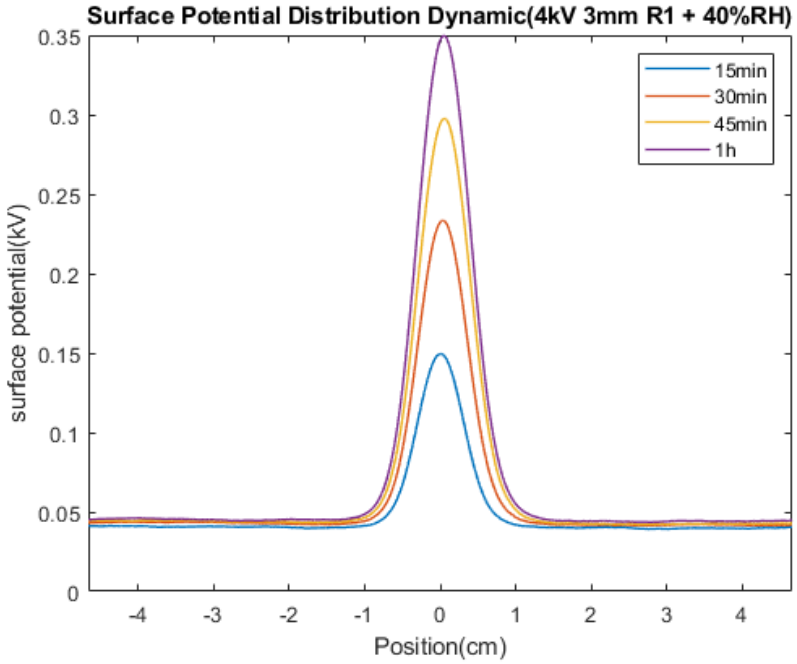

Figure A.25: Potential Variations at 40% RH in Polarity Group (Positive)

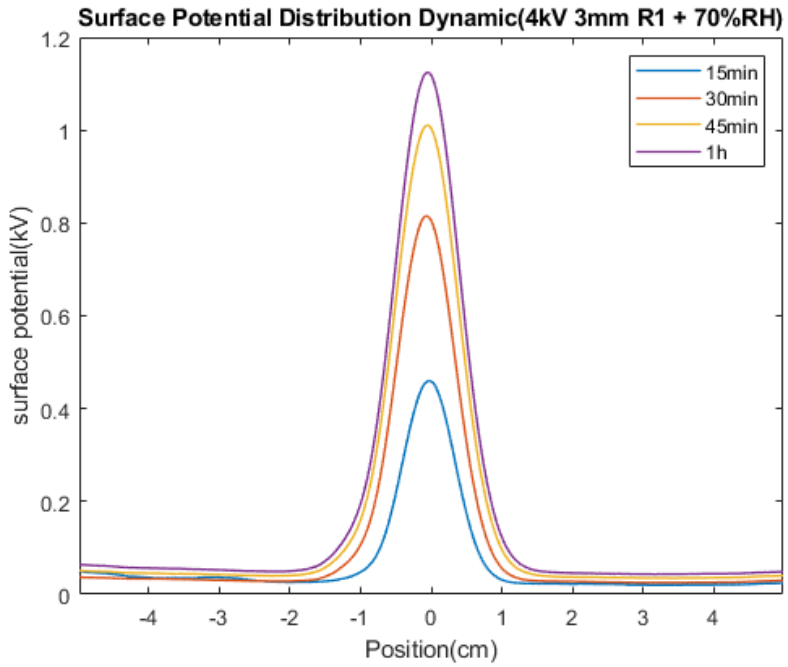

Figure A.26: Potential Variations at 70% RH in Polarity Group (Positive)

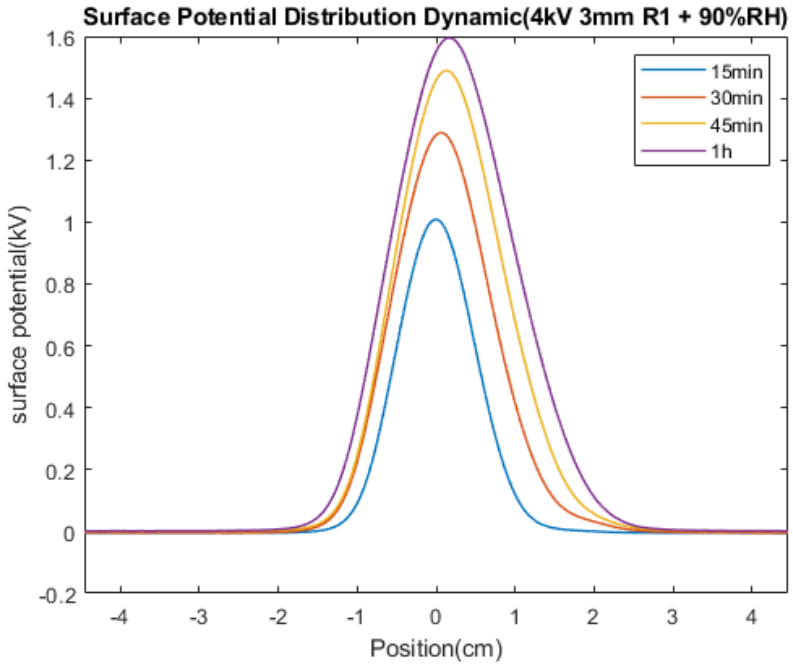

Figure A.27: Potential Variations at 90% RH in Polarity Group (Positive)

Configuration: V3=4kV, L2=3mm, R1=4mm, Negative Polarity

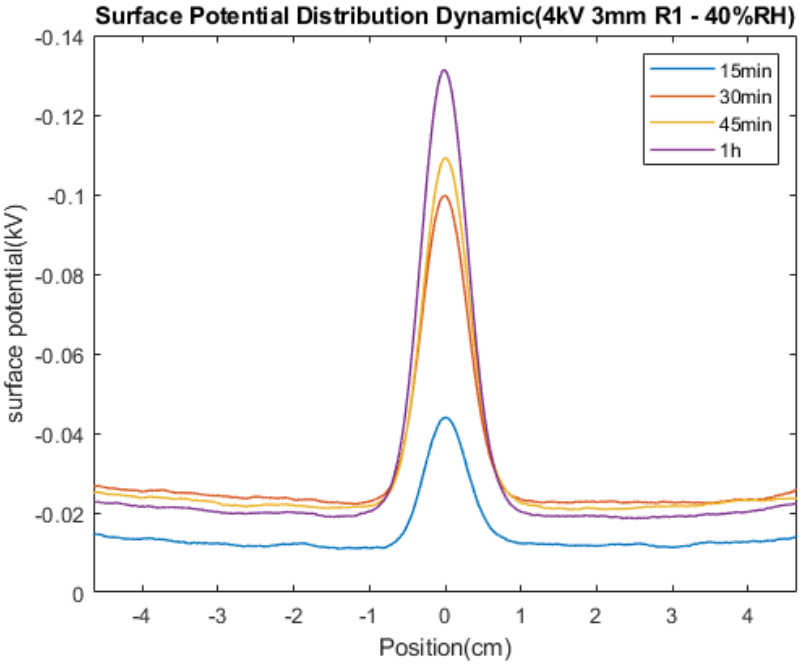

Figure A.28: Potential Variations at 40% RH in Polarity Group (Negative)

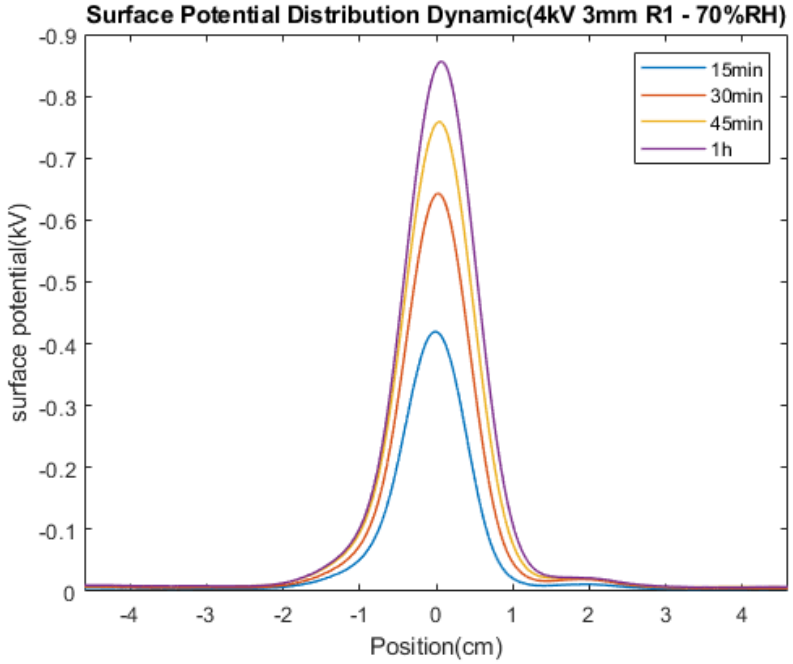

Figure A.29: Potential Variations at 70% RH in Polarity Group (Negative)

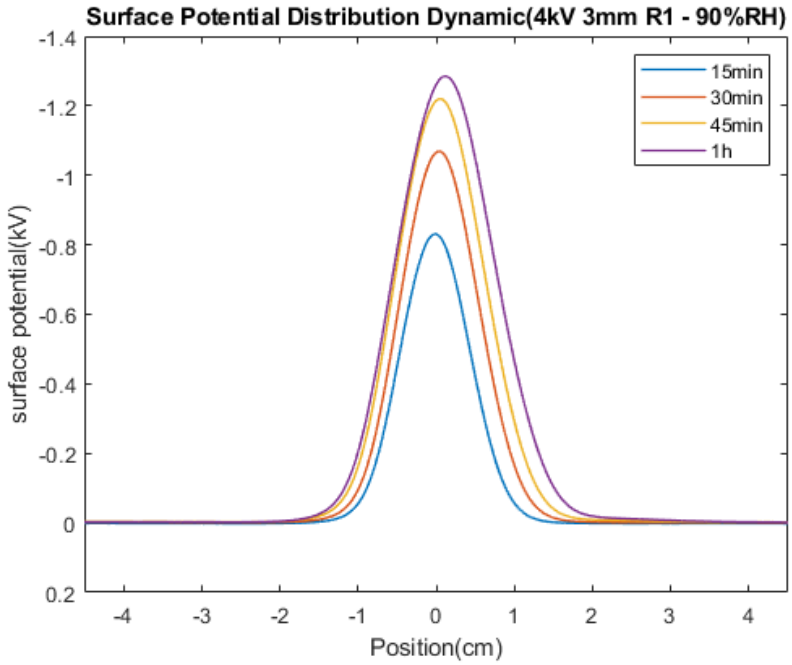

Figure A.30: Potential Variations at 90% RH in Polarity Group (RNegative)

DEPARTMENT OF SOME SUBJECT OR TECHNOLOGY
CHALMERS UNIVERSITY OF TECHNOLOGY
Gothenburg, Sweden
www.chalmers.se

CHALMERS
UNIVERSITY OF TECHNOLOGY